

Generation and Propagation of Inertia–Gravity Waves from Vortex Dipoles and Jets

SHUGUANG WANG*

Department of Atmospheric Sciences, Texas A&M University, College Station, Texas

FUQING ZHANG

Department of Meteorology, The Pennsylvania State University, University Park, Pennsylvania

CHRIS SNYDER

National Center for Atmospheric Research, Boulder, Colorado

(Manuscript received 6 May 2008, in final form 27 October 2008)

ABSTRACT

This study investigates gravity wave generation and propagation from jets within idealized vortex dipoles using a nonhydrostatic mesoscale model. Two types of initially balanced and localized jets induced by vortex dipoles are examined here. These jets have their maximum strength either at the surface or in the middle levels of a uniformly stratified atmosphere. Within these dipoles, inertia–gravity waves with intrinsic frequencies 1–2 times the Coriolis parameter are simulated in the jet exit region. These gravity waves are nearly phase locked with the jets as shown in previous studies, suggesting spontaneous emission of the waves by the localized jets. A ray tracing technique is further employed to investigate the propagation effects of gravity waves. The ray tracing analysis reveals strong variation of wave characteristics along ray paths due to variations (particularly horizontal variations) in the propagating environment.

The dependence of wave amplitude on the jet strength (and thus on the Rossby number of the flow) is examined through experiments in which the two vortices are initially separated by a large distance but subsequently approach each other and form a vortex dipole with an associated amplifying localized jet. The amplitude of the stationary gravity waves in the simulations with 90-km grid spacing increases as the square of the Rossby number (Ro), when Ro falls in a small range of 0.05–0.15, but does so significantly more rapidly when a smaller grid spacing is used.

1. Introduction

Gravity waves propagating vertically from the lower atmosphere are widely recognized to play important roles in a variety of atmospheric phenomena. Known sources of these gravity waves include mountains, moist convection, fronts, upper-level jets, geostrophic adjustment, and spontaneous generation (Fritts and Alexander 2003, and references therein). Among these, jets are

often responsible for generating low-frequency inertia–gravity waves with characteristic horizontal wavelengths of several hundred kilometers, as suggested by many observational studies (e.g., Uccellini and Koch 1987; Sato 1994; Wu and Zhang 2004). Numerous mechanisms for gravity wave generation by jets have been proposed (e.g., Zhang 2004), but such generation remains poorly understood compared to other wave sources such as topography and moist convection. Diagnosing jet-related generation of inertia–gravity waves in observed cases is also often difficult because the jet typically coexists with other potential sources such as surface fronts and moist convection (e.g., Zhang et al. 2001; Plougonven and Teitelbaum 2003).

To focus on essential dynamics of jet-related wave generation, different idealized settings of jets have been proposed in several studies. One approach to simplify

* Current affiliation: Department of Applied Physics and Applied Mathematics, Columbia University, New York, New York.

Corresponding author address: Dr. Fuqing Zhang, Dept. of Meteorology, The Pennsylvania State University, University Park, PA 16802.
E-mail: fzhang@psu.edu

the wave generation scenario is to simulate a jet in the context of developing baroclinic waves (O'Sullivan and Dunkerton 1995; Zhang 2004; Wang and Zhang 2007; Plougonven and Snyder 2007). In this approach, the spontaneous generation of gravity waves associated with the jet within the idealized baroclinic waves occurs in a complex, time-dependent flow, whereas the synoptic-scale background evolves relatively quickly. Snyder et al. (2007, hereafter SMPZ07) took another approach by creating a localized jet that arises naturally within surface-trapped vortex dipoles. They unambiguously identify long-lived inertia-gravity waves emitted by the dipole. The dipole flow supporting the wave generation evolves very slowly in time (up to many inertial periods) and is nearly steady in an appropriate frame of reference. The inertia wave packets were first noticed by Viúdez (2006) and further examined in Viúdez (2007, 2008). In these studies, Viúdez considered vortex dipoles associated with potential vorticity (PV) anomalies in the interior of the flow rather than confined to a horizontal boundary. Despite the simplified setting of the vortex dipole, the continuous generation of inertia-gravity waves from vortex dipoles is qualitatively similar to those in baroclinic waves in the sense that they appear in the jet exit region and propagate in phase with the jet. These slowly evolving vortex dipoles provide a good laboratory to better understand fundamental mechanisms of gravity wave generation by jets.

As an extension of SMPZ07 and Viúdez (2008), this study further explores gravity wave generation in different localized jets settings, including a surface vortex dipole and a dipole maximizing in the midlevel of the atmosphere. Broadly speaking, the spatial structure of simulated waves from the surface vortex dipole is similar to that in SMPZ07 and the structure of waves in the midlevel dipole is similar to that in Viúdez (2007, 2008). However, the current study will have the advantage of directly comparing waves from the surface and midlevel dipoles in a nonhydrostatic mesoscale model. The dependence of the wave amplitude on jet strength is further estimated using slowly amplifying jets that are simulated in distant dipole experiments, in which a cyclone and an anticyclone are initially separated by a large distance but subsequently slowly approach each other and form a vortex dipole. We will stress both similarities and differences of gravity waves in these different types of dipoles and further discuss implications for wave source mechanisms.

This study will also investigate the propagation of gravity waves in the sheared flow in the exit region of localized jets. Past studies show that wave characteristics may change significantly along the propagation path in an inhomogeneous media (Staquet and Sommeria 2002;

Plougonven and Snyder 2005; Lin and Zhang 2008). In the presence of strong horizontal wind variations, Bühler and McIntyre (2005) and an earlier study by Badulin and Shrira (1993) suggested that the wave-capture mechanism is important for wave propagation. Plougonven and Snyder (2005) demonstrated that this mechanism is useful for stratospheric gravity wave packets where strong horizontal deformation and vertical wind shear are found. SMPZ07, however, argued that packets of emitted waves in their simulations propagated too quickly through the jet exit region for wave capture to occur. Our study will further examine the possibility of wave capture by using a ray tracing model that incorporates spatial and temporal variations of the background flow.

The rest of this article is organized into five sections. Section 2 describes experimental design. Wave generation from different types of dipoles is discussed in section 3. Ray tracing analysis is performed in section 4. Dependence of wave amplitude on the Rossby number is explored in section 5 through the distant dipole experiments. A summary and discussion will be presented in section 6.

2. Experimental design

This study employs a nonhydrostatic, compressive, mesoscale model [the fifth-generation Pennsylvania State University-National Center for Atmospheric Research Mesoscale Model (MM5), version 3; Dudhia 1993] to perform all numerical experiments. Ertel potential vorticity (EPV) inversion (Davis and Emanuel 1991) is adopted to create initial conditions for the primitive equation model because it can minimize the adjustment processes due to flow imbalance. The initial EPV anomalies will be introduced once a reference state is defined. Configurations of the initial EPV anomalies along with other important numerical aspects are given below.

a. Vortex dipole initialization

For all experiments, we first specify the reference state with constant static stability $N^2 = 2 \times 10^{-4} \text{ s}^{-2}$ (detailed in the appendix). All thermodynamic variables, including the reference state EPV in a reduced form $Q(z) = -gf \partial\theta/\partial p = -fN^2 / g\theta/\rho$, are thus determined using the reference static stability, where g , f , θ , ρ , and p are gravity, the Coriolis parameter, potential temperature, density, and pressure, respectively. The reference θ increases exponentially with height: $\theta = \theta_o \exp(N^2 z/g)$.

To produce a surface vortex dipole similar to SMPZ07, in experiment SFJET we prescribe a pair of oppositely signed surface temperature anomalies of the same magnitude using a truncated cosine function. The θ anomalies smoothly drop to zero at a circle of 1800 km. The

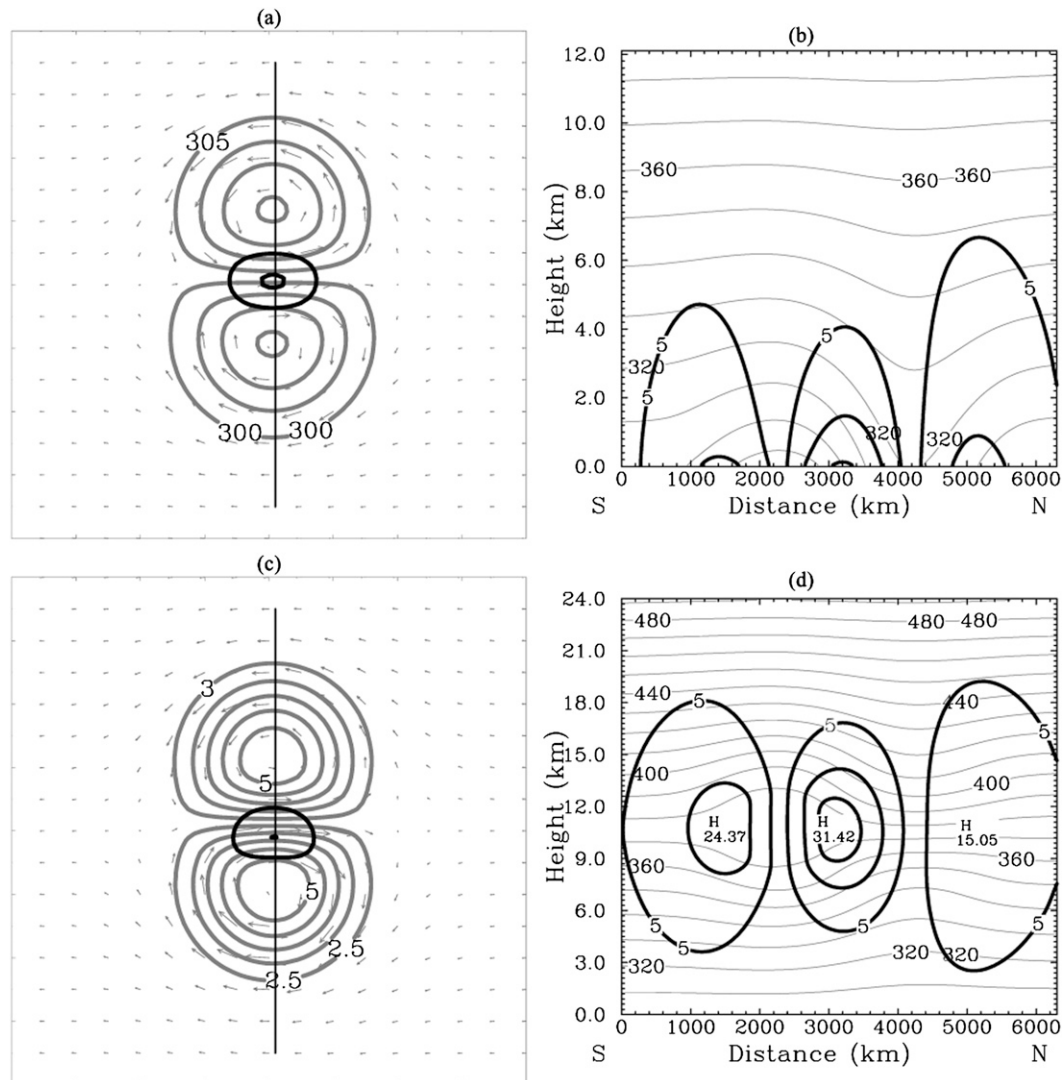


FIG. 1. Initial conditions for (a),(b) SFJET and (c),(d) MDJET. Wind vectors, wind speed [contour interval (CI) is 5 m s^{-1} , with values less than 20 m s^{-1} omitted], potential temperature [CI = (a) 5 and (b) 10 K] for SFJET are plotted (a) at $z = 0.1 \text{ km}$ and (b) along the vertical cross sections indicated by black solid line in (a). (c) Wind vectors, wind speed, potential vorticity [CI = 0.5 PV units (PVU), where $1 \text{ PVU} = 10^{-6} \text{ m}^2 \text{ s}^{-1} \text{ K kg}^{-1}$] at 12 km for MDJET; (d) wind speed and potential temperature along the black line in (c). The distance between ticks in (a) and (b) is 900 km. Note only a small subset of domain is shown on the horizontal planes.

positive (negative) boundary temperature anomalies in Fig. 1a are equivalent to interior positive (negative) potential vorticity anomalies that are associated with cyclonic (anticyclonic) circulations (Hoskin et al. 1985). An initially balanced and localized jet is subsequently obtained through EPV inversion of these dipolar surface temperature anomalies. Figure 1a shows that this localized jet has a maximum wind of 25 m s^{-1} . Using this wind speed and the horizontal scale L of 1800 km (distance between the two vortex cores), the Rossby number ($\text{Ro} = U/fL$) is estimated to be ~ 0.14 . The surface

relative vorticity is also nearly symmetric with a maximum $0.55 f$ ($-0.6f$) in the cyclone (anticyclone) center. A vertical cross section reveals further asymmetry: the horizontal winds in the surface cyclone extend to higher levels than those in the anticyclone (Fig. 1b). This asymmetry is due in part to the larger penetration depth H of EPV anomalies in the cyclone where static stability N is reduced because H and N are related by $H = fL/N$, where L is the horizontal scale.

The experiment MDJET initializes a midlevel vortex dipole with a pair of oppositely signed EPV perturbations

of the same magnitude in the midtroposphere (see details in the appendix). Figures 1c,d show the initial horizontal and vertical structure of MDJET. The wind speed in the anticyclonic (cyclonic) flank is 24.4 (15.1) m s^{-1} (Fig. 1c). For reasons discussed later, the jet core shifts toward the anticyclone. The maximum wind speed in the jet core reaches 31.5 m s^{-1} , rendering an Eulerian Rossby number of ~ 0.18 given the horizontal scale L of 1800 km (distance between the two vortex cores). In both SFJET and MDJET, the Rossby number will remain below 1, suggesting that no inertial stability is occurring in either case. In the surface dipole, the inverted horizontal winds above (and below) the EPV anomalies penetrate higher in the cyclone than the anticyclone. The maximum vorticity reaches $0.45f$ ($-0.75f$) in the center of the cyclone (anticyclone).

The distant dipole experiments (DISTJET) are initialized with the same cyclonic and anticyclonic vortices as in MDJET but are separated by an initial distance of 3600 km between the vortex cores, twice that in MDJET. Because of this large distance, the initial conditions of DISTJET contain no jet (not shown). Nevertheless, a localized jet develops at a later time (see section 5) as the vortices slowly approach each other.

b. Model configurations

All simulations, unless otherwise specified, are configured with two domains through two-way nesting. The 90-km coarse domain is 13 500 km long (x direction), 15 400 km wide (y direction), and 24 km high. The vertical spacing is 200 m for the experiment MDJET but is stretched for SFJET with more vertical levels near the surface. The 30-km fine domain focuses on the dipoles with 241 grid points in both x and y directions. The model top pressure is 10 hPa, or 24 km. To minimize the reflection of gravity waves from boundaries, a Rayleigh-type sponge layer is included near the model top, in addition to the MM5 built-in radiative boundary conditions (Grell et al. 1994). A sponge layer is also included near the bottom boundary for MDJET. MM5 is configured to have zero tendencies at lateral boundaries. The MM5 built-in diffusion scheme (i.e., the deformation-dependent fourth-order form) is applied at interior points for all simulations.

3. Simulated gravity waves from jet dipoles

This section discusses differences in gravity waves between SFJET and MDJET. It is suggested that wave generation is closely related to localized jets. The shift of the localized jet toward the anticyclone in MDJET is discussed. Finally, the relevance of flow imbalance is discussed.

a. Gravity waves from the two types of vortex dipoles (SFJET and MDJET)

The vortex dipoles in SFJET and MDJET drift eastward very slowly with a translation speed of ~ 1.1 and $\sim 1.2 \text{ m s}^{-1}$, respectively. This slow drift arises from the mutual advection of the vortices (Flierl 1987; SMPZ07). In MDJET, because of the stronger wind associated with this cyclone, the dipole jet system as a whole also rotates gradually clockwise, with the primary jet axis turning gradually to the right (e.g., from due east at 0 h in Fig. 1c to east-southeast at 210 h in Fig. 2c). Owing to nonlinear interaction among vortices, both vortices undergo a slow deformation. This is more apparent for the cyclonic vortex, which becomes more elongated along the primary jet axis. In the meantime, the two vorticity centers also draw closer to each other, corresponding to a slight increase in the maximum jet speed and thus a slight increase in the Rossby number. Figure 3b shows the time evolution of the horizontal wind speed along a straight line that always connects the two vorticity centers in MDJET.

Low-frequency inertia-gravity waves appear in both SFJET and MDJET in the exit regions of the localized jets (Figs. 2 and 4). Two groups of upward-propagating jet exit region gravity waves from the SFJET are simulated: one is trapped below ~ 2 km and the other is located from 4 to 8 km. For MDJET, there are also two distinct groups of gravity waves simulated. The gravity waves of primary interest are nearly phase locked with the jet, propagate nearly symmetrically both upward and downward, and are confined to an area 6–16 km above ground level (AGL). A different, transient group of gravity waves also appears in the jet exit region above 16 km and below 6 km (Fig. 2d). These waves weaken gradually and eventually disappear after long integrations (e.g., Fig. 5d) and were thus attributed to initial adjustment by Viúdez (2008). Overall, the jet exit region gravity waves from the SFJET are similar to the upward-propagating waves at and above the jet core level in MDJET. Waves appearing in the immediate exit region of the jet core in both simulations have phase lines that are nearly stationary with respect to the jet. The similarity of waves in both MDJET and SFJET further indicates that these waves are robust phenomena, regardless of different models or different boundary conditions used in these studies.

Nevertheless, there are noticeable differences between the characteristics of the gravity waves in the jet exit region of SFJET and MDJET. First, Fig. 4b shows that phase lines of wave packets at the leading edges in MDJET are mostly parallel to the lines of constant wind speed, which is similar to waves analyzed

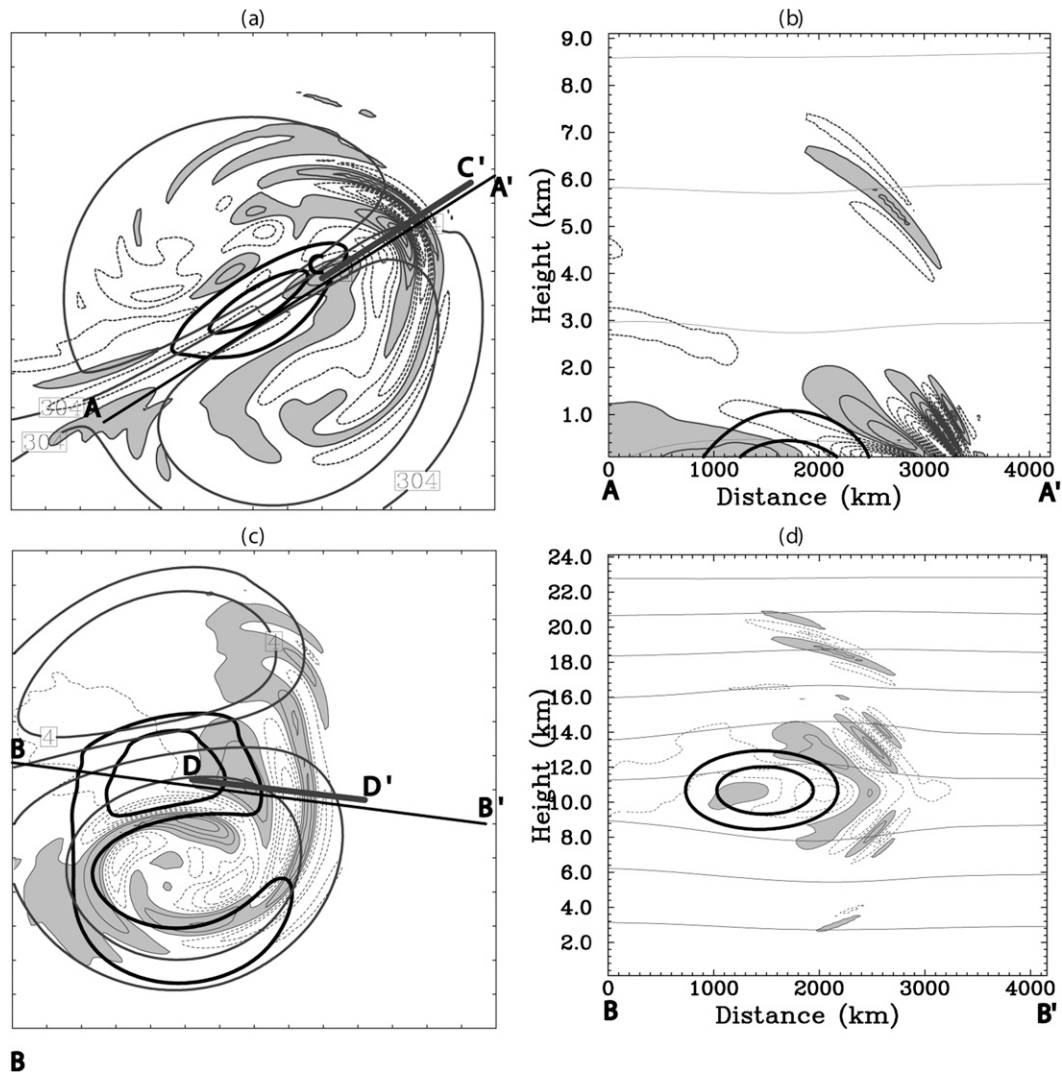


FIG. 2. Simulated horizontal divergence and wind speed for (a),(b) SFJET and (c),(d) MDJET. (a),(c) Horizontal divergence ($CI = 0.01 \times 10^{-4} \text{ s}^{-1}$; positive, shaded; negative, dashed), potential temperature (gray; $CI = 20 \text{ K}$) and wind speed (black lines; $CI = 5 \text{ m s}^{-1}$; values $< 20 \text{ m s}^{-1}$ omitted) on the 30-km domains for (a) SFJET at 0.5 km valid at 210 h and (c) MDJET at 12.5 km at 210 h. (b),(d) Divergence for (b) MDJET and (d) SFJET at the vertical cross sections indicated by black solid lines in (a) and (c), respectively. The distance between ticks in (a) and (b) is 900 km.

in Viúdez (2008). In contrast, this is not true for wave packets in SFJET as seen in Fig. 4a, which is similar to Fig. 10 in SMPZ07. Figure 4b also suggests that wave capture may be an important factor, which will be further discussed through the use of a ray tracing model.

Second, the wave pattern is more asymmetric about the dipole axis in MDJET, with a significant portion extending to the anticyclone. The preferred occurrence of waves in the anticyclonic side persists over the entire simulation of MDJET. However, this is not surprising if we consider that the localized jet shifts to the anticyclone in the midlevel dipole from the beginning and also persists (Figs. 3a,c). The shift of the initial jet toward the

anticyclone in MDJET results from the prescribed EPV distribution and induced asymmetry between anticyclones and cyclones. The EPV may be written as

$$Q = \frac{g}{\rho\theta_0} \left[(\zeta_z + f) \left(N^2 + \frac{\partial b}{\partial z} \right) + \zeta_x \frac{\partial b}{\partial x} + \zeta_y \frac{\partial b}{\partial y} \right] \\ = \frac{g}{\rho\theta_0} \left(fN^2 + \zeta_z N^2 + f \frac{\partial b}{\partial z} + \zeta_x \frac{\partial b}{\partial x} + \zeta_y \frac{\partial b}{\partial y} \right), \quad (1)$$

where b is buoyancy and ζ_x , ζ_y , and ζ_z are the three components of vorticity. The first term (the product of planetary vorticity f and the reference static stability) is the reference EPV and the subsequent terms are PV

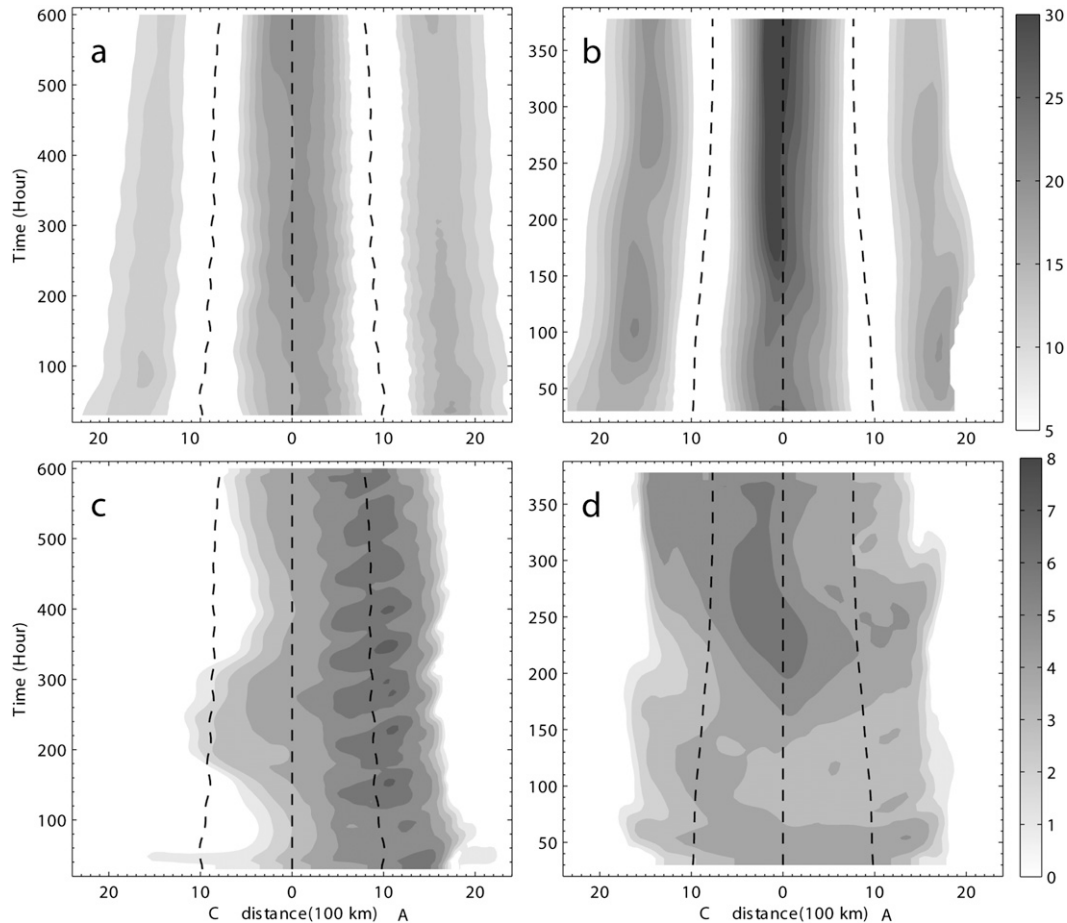


FIG. 3. Hovmöller diagrams of wind speed along the centers of the cyclone and the anticyclone for (a) MDJET and (b) SFJET. The centers of vortex dipoles (indicated by black dashed lines) are defined by (a) the perturbation potential temperature contours of -5 and 4 K at 11.6 km for MDJET and (b) contours of ± 10 K at 0.5 km for SFJET. Contours of wind speed less than 5 m s^{-1} are omitted. Note that the vortex centers are symmetric about the middle dashed line. (c),(d) Wave variances for (c) MDJET and (d) SFJET. See text for details.

anomalies from the reference EPV, with the second and third terms being linear and the rest being quadratic. From scale analysis (Rotunno et al. 2000), the linear terms are one order smaller than reference EPV [$\sim O(\text{Ro})$] and the quadratic terms are $O(\text{Ro}^2)$ (details in the appendix). Because the wind profile near the vortex is near zero, the horizontal terms are very small and thus will not be considered here. The sign of the linear terms depends on vorticity; it is negative in anticyclones and positive in cyclones. In contrast, the quadratic term $\zeta_z \partial b / \partial z$ is always positive in both cyclones and anticyclones. As a result, the relative vorticity and static stability are stronger in the anticyclone than in the cyclone, regardless of the equal magnitude of the prescribed EPV anomalies. According to Stokes' theorem, stronger vertical vorticity in the anticyclone is associated with strong wind speed (Fig. 1c), which induces a shift of the localized jet (or wind contours) toward the anticyclone.

Time evolution of the localized jet and wave variance are compared between the midlevel dipole and the surface dipole. Figure 3 shows the Hovmöller diagram of wind speed and wave variance (defined below) along the line connecting the vortex cores. The vortex core is defined as the geometric center of EPV anomalies (± 2 PVU) at 12.5 km for MDJET and potential temperature anomalies (± 10 K) at the surface for SFJET. This line and one of its perpendiculars (i.e., the dipole axis) are chosen as the x and y axes and define a frame with the origin located at the midpoint of vortex cores. In general, the vortex dipole and the localized jet remain relatively stationary throughout the integration time period. To quantify how much wave activity varies along the direction perpendicular to the dipole (y) axis, we define wave variance as the variance of filtered divergence along the dipole axis. The filtered divergence is obtained by applying a 2D high-pass filter with a 240 -km

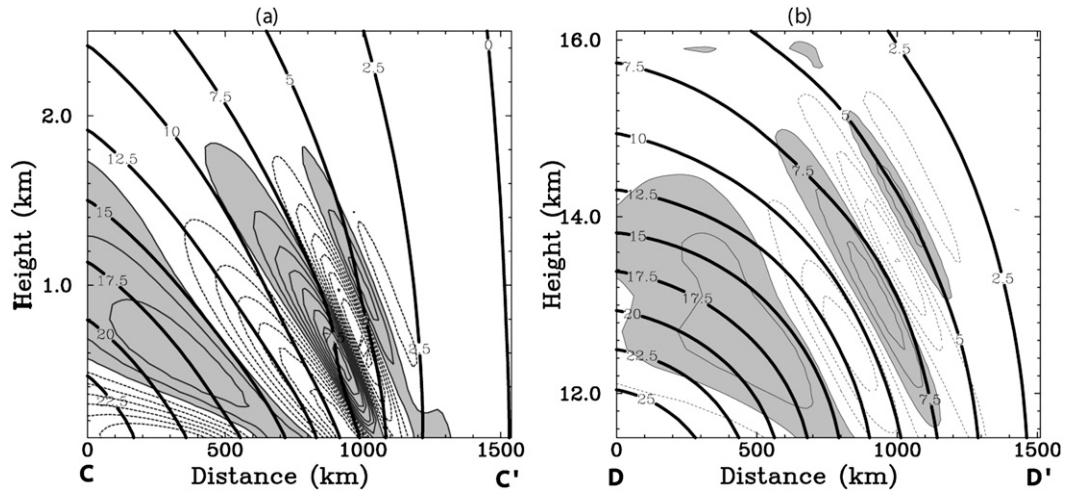


FIG. 4. Simulated horizontal divergence ($CI = 0.01 \times 10^{-4} \text{ s}^{-1}$; positive, shaded; negative, dashed) and sectional parallel wind speed ($CI = 2.5 \text{ m s}^{-1}$; solid) at 210 h for (a) SFJET along the cross section CC' indicated by the gray line in Fig. 2a and (b) MDJET along DD' indicated by the gray line in Fig. 2c.

cutoff wavelength to horizontal divergence at 12.5 km. This digital filtering technique is a 2D convolution operation between the data and a chosen window. It is the same as in Wang and Zhang (2007), except that a Chebyshev window (41×41 grid points) is adopted here. Figures 3c,d show the time evolution of wave variance. For MDJET, most wave variance is found near the anticyclones where the curved jet is shifted. In the surface dipole they are found close to the cyclones, where slightly stronger wind is also found. The phase locking between the jet and the gravity waves in the exit region in SFJET and MDJET suggests that the generation of these gravity waves is related to the localized jets. Close inspection of wave variance in Figs. 3c,d shows that wave variance increases as the jet between the dipoles slowly evolves (Figs. 3a,b).

b. Gravity waves and flow imbalance from the midlevel dipole

The gravity waves remain nearly stationary in the moving frame of the vortex dipole and their energy propagates upward (downward) downstream of an area of divergent (convergent) flow above (below) the jet level (Fig. 2a). The phase of these upward- and downward-propagating waves differs because of the changing sign of vertical wavenumber, whereas the amplitude probably differs because of decreasing density with increasing height. The most conspicuous wave bands in Figs. 2c,d have weak amplitude, with maximum divergence reaching $0.03 \times 10^{-4} \text{ s}^{-1}$ and a horizontal (vertical) wavelength of ~ 300 km (2 km). Using the dispersion relation for inertia-gravity waves and a background static stability $N^2 = 2 \times 10^{-4} \text{ s}^{-2}$, the roughly

estimated wave frequency is $1.4f$, close to the inertial frequency. The wave frequency has been analyzed in SMPZ07 and Viúdez (2008). The horizontal and vertical wavelengths and the intrinsic frequency of these waves are larger than those of the waves simulated in the surface dipole of SMPZ07 (70 km, 520 m, and $1.1f$). The transient wave packets further away from the jet core level (above 16 km or below 6 km) have nonstationary phase lines that can barely be separated from the phase-locked waves near the jet core at 90 h (Fig. 5b). The intrinsic frequency of these transient waves tends to approach the inertial limit at later times, and they eventually disappear in the divergence fields after ~ 540 h (Fig. 5d). Figure 5 also shows a slight strengthening of the localized jet and a slight increase in wave amplitude from 90 to 540 h, in line with Hovmöller diagram in Fig. 4. We will quantify the dependence of wave amplitude on jet strength in section 5.

The weak wave emission from vortex dipoles discussed above is different from jet front systems studied by Zhang (2004) in that baroclinic waves evolve much more quickly (a few inertial periods) and a continuous strengthening flow imbalance is generated. Here, flow balance refers to a physically realizable flow state in the absence of any hydrodynamic instabilities or gravity waves, and flow imbalance is any departure from the balance in consideration (Hoskins et al. 1985). We use ΔNBE as a measure of flow imbalance (Zhang et al. 2000),

$$\Delta NBE = 2J(\psi_y, -\psi_x) + f\zeta - \alpha \nabla^2 P, \quad (2)$$

where ψ , ζ , and α are streamfunction, relative vorticity, and specific volume, respectively. However, because

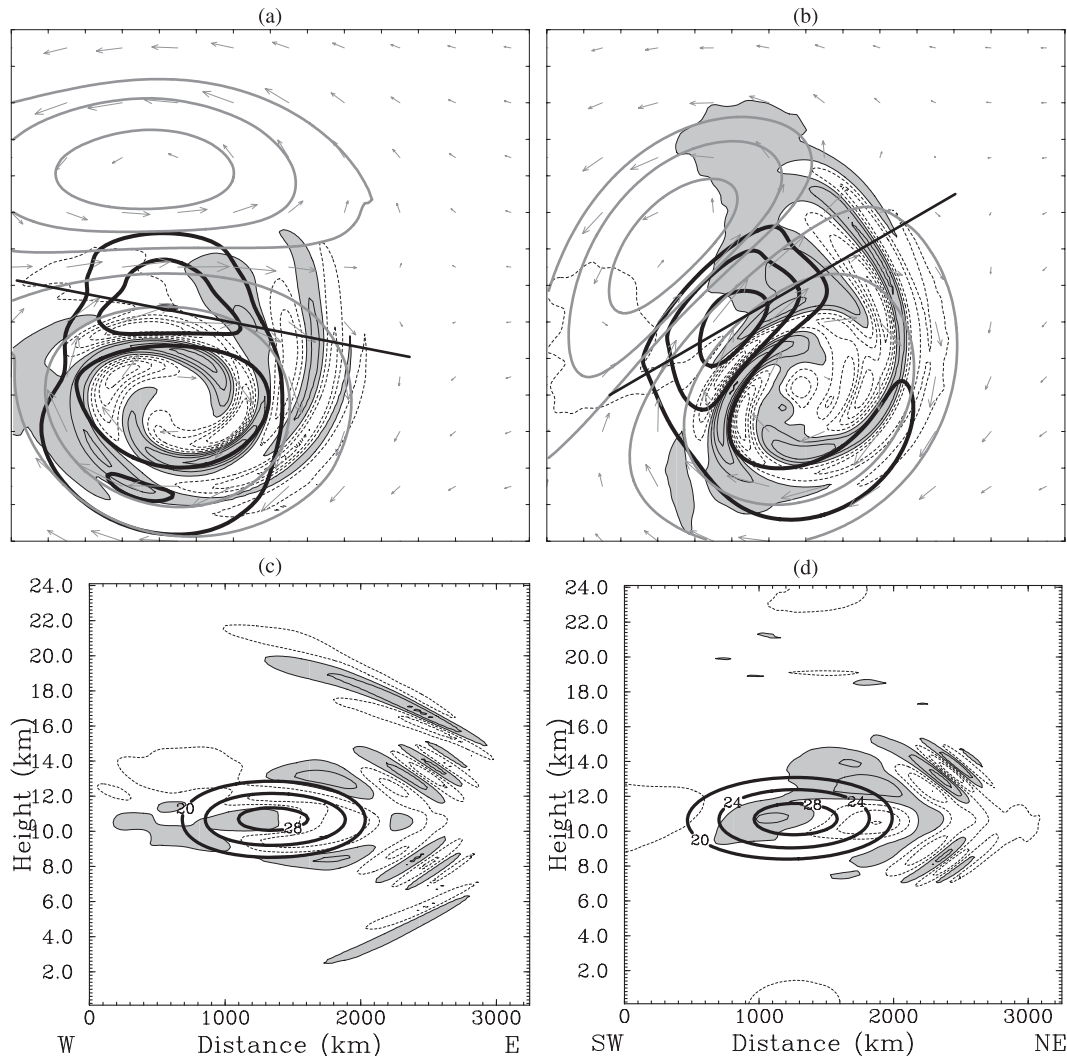


FIG. 5. Horizontal divergence (positive, shaded; negative, dashed; $CI = 0.01 \times 10^{-5} s^{-1}$), wind speed (black; $CI = 5 m s^{-1}$, starting from $20 m s^{-1}$) and PV (gray; $CI = 1 PVU$) at 12.5 km from MDJET valid at (a) 90 and (b) 540 h, and along the cross sections at (c) 90 and (d) 540 h with their location indicated by black lines in (a) and (b), respectively. The distance between adjacent ticks in (a) and (b) is 300 km.

stronger flow imbalance usually leads to stronger gravity wave emission, ΔNBE may also be considered as a measure the potential of a flow to generate gravity waves.

Figure 6 shows a snapshot of the flow imbalance (ΔNBE) at 210 h, when ΔNBE reaches $2 \times 10^{-10} s^{-2}$ in the jet exit region downstream of an area of negative ΔNBE . Waves with upward and downward group velocity appear above and below this area of negative ΔNBE (Fig. 6b). Compared with gravity waves from the idealized baroclinic wave simulations (Zhang 2004), both the magnitude of ΔNBE and the gravity waves are much weaker, possibly because of the absence of baroclinic instabilities in the dipole simulations. However, it is not clear from these diagnostics how the waves are

related to flow imbalance (Zhang 2004; Plougonven and Zhang 2007).

Figure 7 shows the unbalanced potential temperature and relative vorticity at 210 h. The unbalanced flow is recovered by subtracting the balanced flow from the total flow, whereas the balanced flow is obtained following the same procedures of EPV inversion as in Davis and Emanuel (1991). Consistent with the flow imbalance diagnosis in Fig. 6, the unbalanced flow is very weak compared with the total flow and the balanced flow. Besides the wave signals in the jet exit regions, unbalanced flow seems to be stronger in the anticyclones than in the cyclones, which could be due to wave trapping (as discussed in the ray tracing analysis; see below).

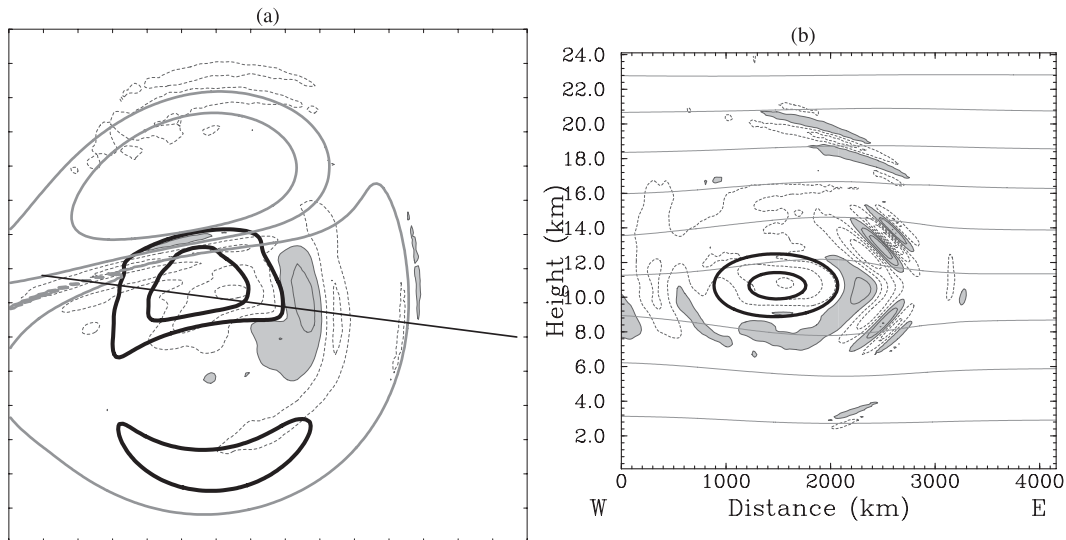


FIG. 6. ΔNBE ($CI = 0.01 \times 10^{-8} \text{ s}^{-2}$; positive values, shaded; negative values, dashed lines) at 210 h in MDJET is plotted (a) at 10.5 km and (b) along the cross section indicated by the straight line in (a).

4. Ray tracing

Ray tracing of wave packets following Lighthill (1978) can be used to study wave refraction due to variations of the background flow. Some authors have applied ray tracing to investigate gravity wave propagation in three-dimensional flows (e.g., Dunkerton and Butchart 1984; Marks and Eckermann 1995). Lin and Zhang (2008) studied the wave characteristics along rays of gravity waves in the baroclinic jet front systems simulated in Zhang (2004). Here, we will use the Gravity-Wave Regional or Global Ray Tracer (GROGRAT; Marks and Eckermann 1995; Eckermann and Marks 1997), a numerical ray tracing model, to examine the effect of the strong flow deformation on the propagation properties of jet exit region gravity waves. Specifically, we seek to understand the following questions using the ray tracing technique: 1) How do wave parameters change when rays are initialized using the values observed in simulated wave packets? 2) How much does the deformation influence the change in characteristics of waves propagating through the jet exit region? 3) Is the wave-capture mechanism discussed in the introduction occurring in MDJET? Does that depend on the initial parameters such as initial frequency of the wave packet? To our knowledge, the wave capture mechanism has not been evaluated using a ray tracing model that accounts for the spatial and temporal variations of the winds.

In this section, rays initialized with the observed wavelength but different horizontal azimuthal angles at different initial locations are first used to study the change of wave parameters along the propagation path. Rays with different initial frequency are studied to further

clarify the role of flow deformation and the possibility of wave capture. Finally, the effect of strong vortical motion in the anticyclonic and cyclonic regions is discussed.

a. Ray tracing model

The ray tracing in GROGRAT is based on the dispersion for plane waves:

$$\omega_i^2 = (\omega - uk - vl - wm)^2 = \frac{N^2(k^2 + l^2) + f^2(m^2 + \alpha^2)}{k^2 + l^2 + m^2 + \alpha^2}, \quad (3)$$

where ω_i and ω are intrinsic frequency and absolute frequency; k , l , and m are three components of wave-numbers; u , v , and w are the components of the spatially and temporally varying background flow; and $\alpha = H^2/4$, where H is the density scale height.

The ray tracing model requires the initial wave parameters in the augmented parameter space (k , l , m , x , y , z). In this study, the initial rays are located within the jet exit region. The horizontal wavelengths are several hundred kilometers and the initial intrinsic frequency is a few times the Coriolis parameters. Ray integration stops based on any of the following conditions: 1) their vertical group velocity reaches some a chosen value (10^{-5} m s^{-1} in this study), 2) integration reaches the time limit such that background wind is not available anymore, 3) rays reach the boundary of the physical domain of the wind data, or 4) the Wentzel-Kramers-Brillouin (WKB) conditions are violated (Lin and Zhang 2008). In most cases it takes at most a few inertial periods for rays to travel out of jet region of strong flow

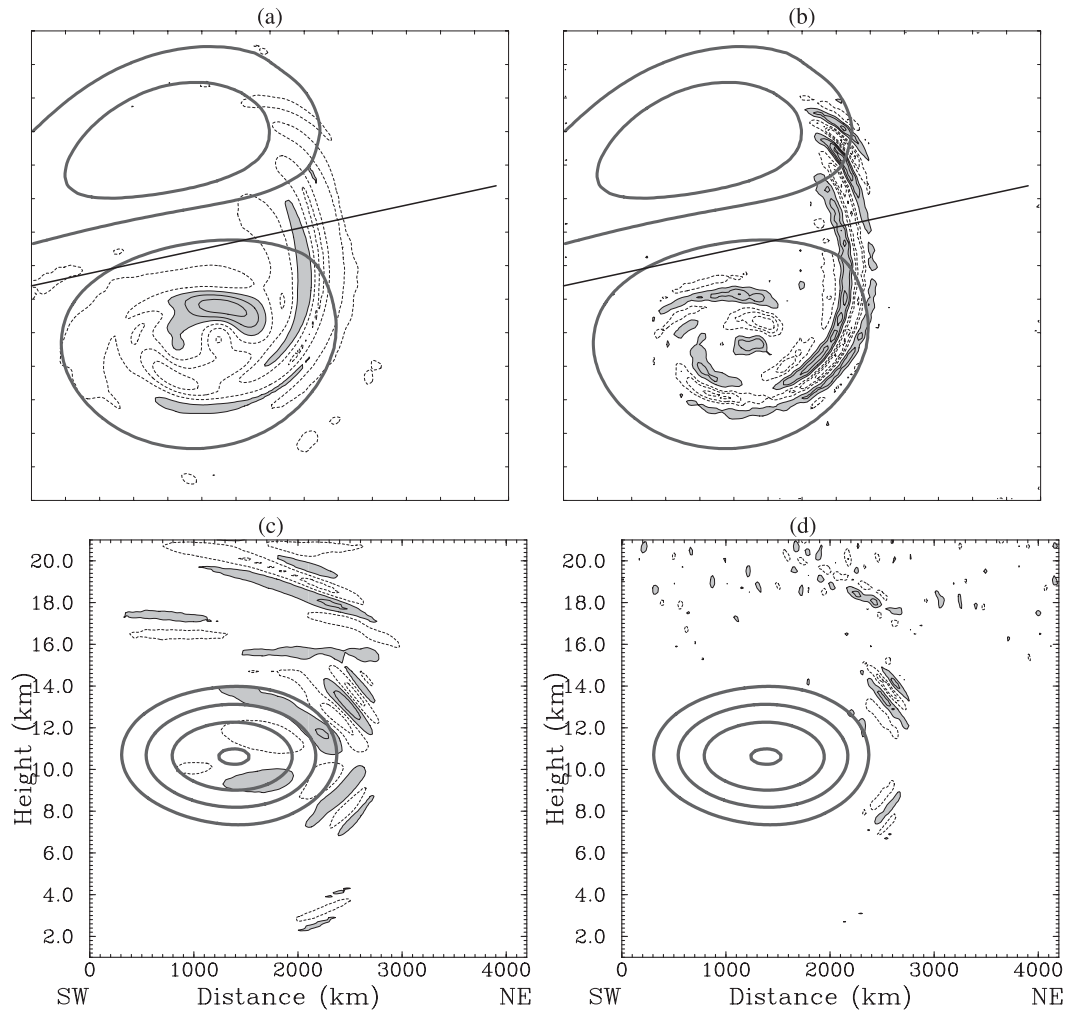


FIG. 7. (a) Unbalanced potential temperature ($CI = 0.05 \text{ K}$) and (b) unbalanced relative vorticity ($CI = 0.008 \times 10^{-5} \text{ s}^{-1}$) at 13.5 km, overlapped on potential vorticity ($CI = 1.5 \text{ PVU}$) at 11.5 km. (c) Unbalanced potential temperature ($CI = 0.05 \text{ K}$), and (d) unbalanced relative vorticity ($CI = 0.008 \times 10^{-5} \text{ s}^{-1}$) and wind speed ($CI = 5 \text{ m s}^{-1}$; values less than 15 m s^{-1} depressed) along the vertical cross sections indicated by thick lines in (a) and (b), respectively.

deformation. For the results discussed, the WKB conditions are all satisfied.

b. Rays initialized at different locations with different horizontal azimuthal angles

Four upward-propagating rays are first released in the jet region to investigate the changes of wave parameters along ray paths. Two rays, S1 and S2, are released from the same location in the jet exit region at 12 km; another two rays, N1 and N2, start from a location displaced to the north of S1 and S2 by 150 km. The rays N1 and N2 have initial horizontal wave vectors parallel to the x axis (and also nearly parallel to the jet axis), whereas S1 and S2 have initial wave vectors making an angle of 45° with

the x axis and pointing southwest. The four rays have an initial horizontal wavelength of 550 km and intrinsic phase speed of 2 m s^{-1} ; the other initial ray parameters are derived from these two values. The rays S1 and N2 are chosen such that they have initial wave parameters close to that of the wave packet observed in simulated wave packets (details not shown). The initial locations, frequency, wavelength, and group velocity are also indicated in Fig. 8 as the rays are released at 12 km.

Figure 8a shows that these rays can travel 1000 km horizontally and as high as 16 km vertically. During their propagation, the initial horizontal wavelength of 550 km decreases to below 400 km at the height of 14 km and to below 200 km at 15 km (Fig. 8c). The vertical

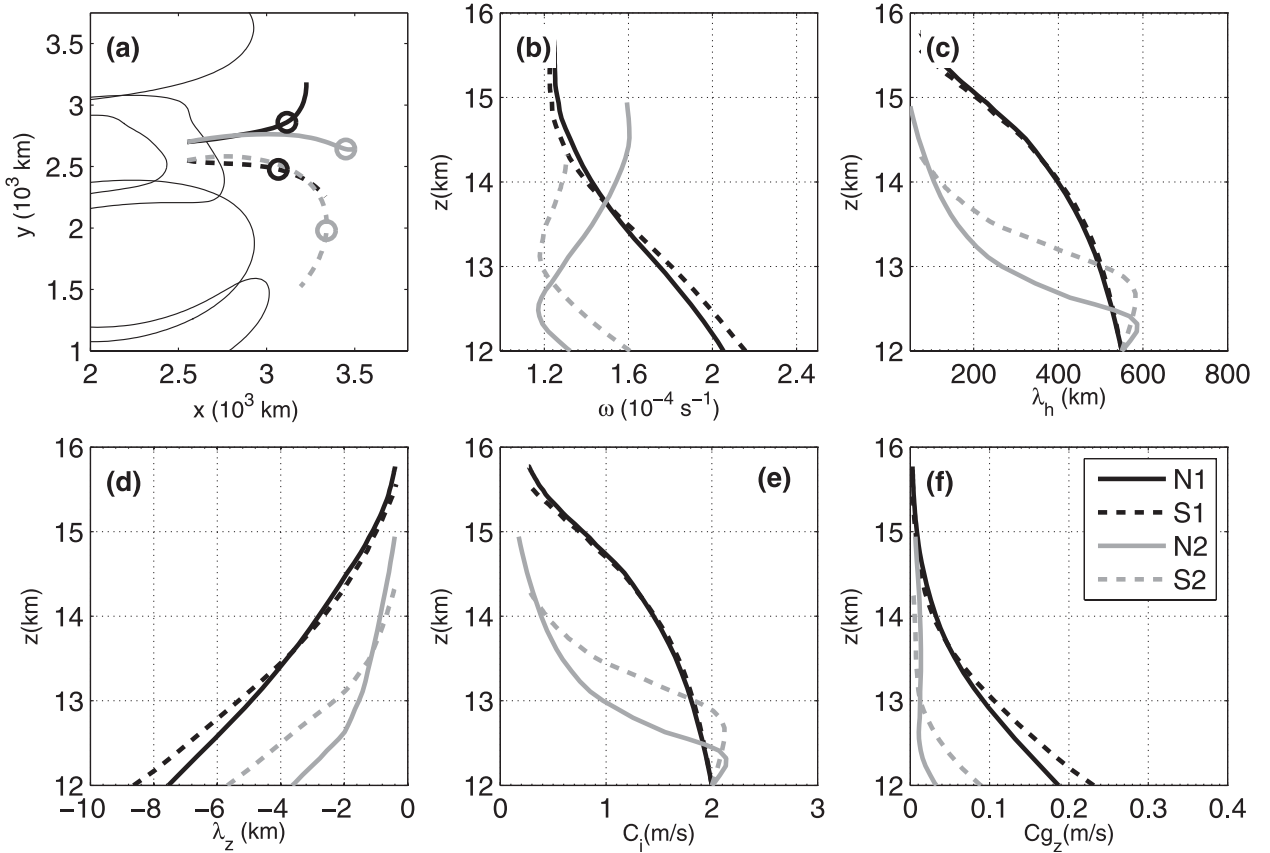


FIG. 8. (a) Ray paths in the horizontal views overlapped on wind speed contours (25 m s^{-1} and 30 m s^{-1}) and perturbation potential temperature ($\pm 4 \text{ K}$) on 11.6 km ; (b) intrinsic frequency, (c) horizontal wavelength, (d) vertical wavelength, (e) intrinsic horizontal phase velocity, and (f) vertical intrinsic group velocity. See text for details.

wavelength also decreases below less than 2 km (Fig. 8d). The intrinsic frequency approaches the inertial limit of gravity waves with a value less than $1.5f$ (Fig. 8b), which is close to the suggested value $\sqrt{2}f$ (Bühler and McIntyre 2005; Plougonven and Snyder 2007). The phase speed relative to the mean wind (C_i) decreases to close to zero (Fig. 8e), indicating the possible horizontal critical levels where the ground-based phase speed matches the mean wind. The decreasing vertical group velocity also suggests the presence of critical levels (Fig. 8f). The inertial critical levels are expected when upward/downward waves propagate far away from the jet core to the levels where winds satisfy $|u - c| = f/k$, where u and c are the wind speed and the phase speed and k is the horizontal wavenumber.

The shrinkage of wavelengths is similar to the wave capture mechanism discussed by Badulin and Shrira (1993) and Bühler and McIntyre (2005). This mechanism predicts that a specific wind structure that has constant horizontal deformation and constant vertical wind shear can effectively select the intrinsic frequency

and determine the spatial structure of wave packets. Specifically, the horizontal wave vectors tend to align with the contraction axis of the local wind, whereas the tilt of wave vectors tends to converge to a value given by the ratio of vertical shear and deformation. Here, strong deformation and wind shear are indeed present in the jet exit region of the three-dimensional dipole flows.

One can assess the capture mechanism using the ray tracing model. The wave capture argument predicts that the vertical tilt and horizontal azimuth of wave vectors are determined by the local contraction axis at large times. The vertical tilt γ of the wave vector is

$$\tan(\gamma) = \nabla_{\text{contr}} U / U_z, \quad (4)$$

where U is the horizontal wind along the contraction axis of the deformation field, $\nabla_{\text{contr}} U$ represents its gradient along the direction of the local contraction axis, and U_z is the vertical gradient of U . The local contraction axis has the horizontal azimuthal angle α , defined through $\tan(2\alpha) = (v_x + u_y) / (u_x - v_y)$, where u

and v are wind components in the x and y directions, respectively.

The influence of flow deformation can be quantified by the stretching rate D , defined as the maximum eigenvalue of the matrix

$$\begin{pmatrix} u_x & v_x \\ u_y & v_y \end{pmatrix};$$

$$D = \max[(u_x + v_y \pm \sqrt{(u_x - v_y)^2 + 4u_y v_x})/2]. \quad (5)$$

Assuming vertical velocity is very small and the static stability variations is negligible, and given the initial values of (k, l) , this matrix determines the horizontal wavenumber vector (k, l) through the equation (Bühler and McIntyre 2005)

$$\frac{d}{dt} \begin{pmatrix} k \\ l \end{pmatrix} = - \begin{pmatrix} u_x & v_x \\ u_y & v_y \end{pmatrix} \begin{pmatrix} k \\ l \end{pmatrix}. \quad (6)$$

The stretching rate reduces to Eq. (3.8) in Bühler and McIntyre (2005) if the flow is horizontally nondivergent. Because the local flow gradient (u_x, u_y, v_x, v_y) is changing along the rays, the stretching rate varies and should be regarded as an instantaneous growth rate of horizontal wavenumber. If the stretching rate is positive (negative) and wave vector makes an angle less than $\pi/4$ with the deformation axis, the magnitude of wave vector increases (decreases) and horizontal wavelength decreases (increases).

Figure 9 shows the time series of stretching rate along the four ray paths in Fig. 8. Here, the stretching rate is calculated using the local wind gradient. The stretching rate of these four rays starts from almost the same values and drops continuously along the ray paths. When $|U_z/\nabla_{\text{contr}}U - m/k|$ is minimal (the circles indicated in Fig. 8a) for these rays, the time span is ~ 30 h for rays N1 and S1 and ~ 15 h for rays N2 and S2. The wavenumber ratio m/k approaches ~ 200 for N1 and S1 but experiences rapid changes for N2 and S2. Figure 9c shows that $U_z/\nabla_{\text{contr}}U$, the anticipated vertical tilt by the wave capture arguments, approaches m/k (~ 200) for N1 and S1 but not for N2 and S2. Given more time, m/k and $U_z/\nabla_{\text{contr}}U$ become closer for N2 but not for S2 because the wave packet S2 eventually propagates into the anticyclonic region (Fig. 8a). Therefore, S1, N1, and N2 approach wave capture before ray integrations stop, but S2 and N2 do not.

The ray tracing results of S1 and N1 are consistent with the MM5 results because phase lines of the wave packet are mostly parallel to lines of constant wind speed (Fig. 3b). As discussed in SMPZ07, the wave

capture is a long-term asymptotic result. Wave packets propagate through varying winds in a limited time, such that wave capture may not occur for all wave packets entering the region of strong flow deformation (such as S2).

c. Influence of flow deformation on rays with different initial frequency

The influence of flow deformation on wave packets is further demonstrated by considering rays with different initial frequency. Figure 10 examines the rays released at the same location as S1 with the same horizontal wavelength (550 km) and the same horizontal angle as S1. These rays are initialized by different initial intrinsic frequencies that are evenly distributed between f and $4.5f$. Figure 10a shows the ray paths projected on the horizontal plane. The set of rays with initial frequency between f and $1.5f$ will be referred to as R1, while the sets of rays with frequencies $1.5f$ – $2.5f$, $2.5f$ – $3.2f$, and $3.2f$ – $4.5f$ will be referred to as R2, R3, and R4, respectively. Rays in R1 and R2 mostly propagate east or south. Rays in R3 and R4 propagate north and west. Figure 10b shows the variation of intrinsic frequency versus height, indicating that the intrinsic frequency ω_i of rays in R1 and R2 quickly reaches $\sim 1.4f$, while that for R3 reaches $1.1f$; and ω_i of rays in R4 does not converge before the rays travel up to 19 km, where the flow deformation is very small compared to the levels 2–3 km above the jet core. The stretching rate following these rays is shown in Fig. 10c. Among the four groups of rays, the stretching rate is clearly the largest for R1 and the smallest for R4. This demonstrates that the wave packets with smaller frequency are more strongly influenced by the flow deformation. On the other hand, higher-frequency waves have larger group velocities and escape faster; hence, the wave capture mechanism is less effective on these wave packets.

The tilt indicated by m/k from the ray tracing model is further compared with $U_z/\nabla_{\text{contr}}U$, which is the anticipated tilt by the wave capture argument. Figure 10d shows m/k versus $U_z/\nabla_{\text{contr}}U$ for these rays. The circles in Fig. 10 indicate that the difference between $U_z/\nabla_{\text{contr}}U$ and m/k , $|U_z/\nabla_{\text{contr}}U - m/k|$, is minimal before the ray calculation is terminated. During wave capture, $U_z/\nabla_{\text{contr}}U$ along a ray should approach m/k (i.e., the paths in Fig. 10d stay close the diagonal). Rays in R1–R3 cross the diagonal line, indicating that $U_z/\nabla_{\text{contr}}U$ equals m/k at some point of the ray path. Among R1–R3, only rays in R2 stay close to the diagonal after crossing the diagonal line, suggesting good agreement between the ray tracing model and the wave capture. For rays in R4, there is no tendency to approach the diagonal line over the time interval considered, indicating that wave capture is not occurring.

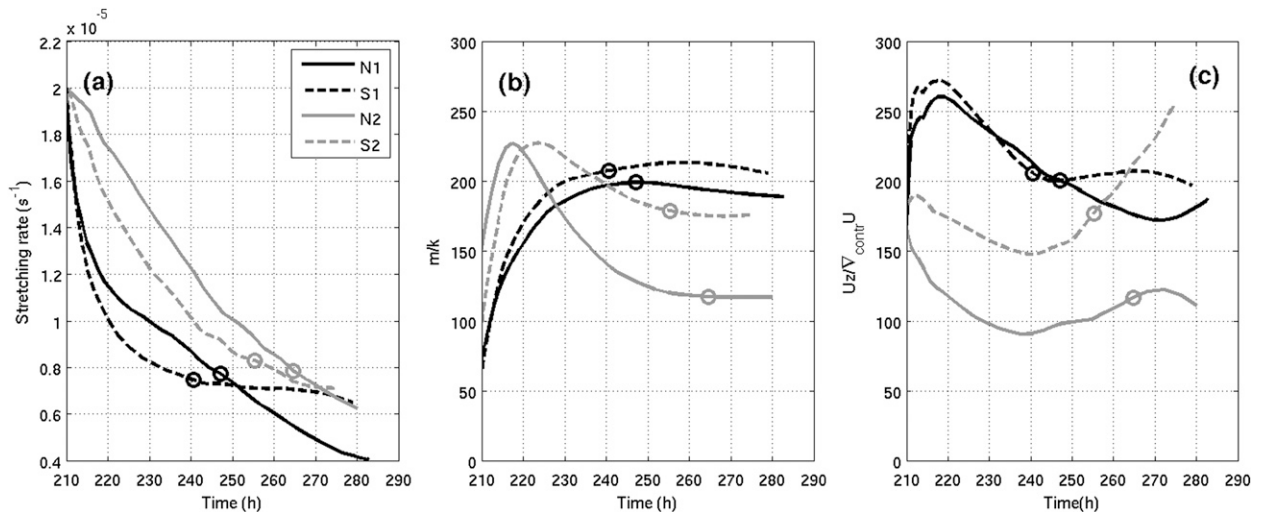


FIG. 9. (a) Stretching rate, (b) m/k , and (c) $U_z/\nabla_{\text{contr}}U$ along the four ray paths in Fig. 8.

The time span for these rays to reach the smallest difference between $U_z/\nabla_{\text{contr}}U$ and m/k can be found in Fig. 10c. R1 has a time span of 25–35 h starting from 210 h. The strong flow deformation quickly forces the wave packets converge to values anticipated by the wave capture. After passing this point (circles in Fig. 10d), R1 continues to travel into anticyclonic region (Fig. 10a) and the wave tilt m/k does not agree with $U_z/\nabla_{\text{contr}}U$. R2 has a longer time span of 30–60 h. After reaching the point where $U_z/\nabla_{\text{contr}}U$ is the smallest, rays in R2 stay in the jet exit region and the stretching rate does not fall below $0.5 \times 10^{-5} \text{ s}^{-1}$ (Fig. 10c). Thereafter, m/k agrees well with $U_z/\nabla_{\text{contr}}U$. Rays in R3 have an even longer time span of 70–80 h before reaching the smallest difference between $U_z/\nabla_{\text{contr}}U$ and m/k . Afterward, rays in R3 almost stop their vertical propagation and travel northward, where the stretching rate is very small (Fig. 10c). For rays in R4, the time it takes for rays to travel out of the domain top (19 km) is less than 30 h. The smallest difference between $U_z/\nabla_{\text{contr}}U$ and m/k is achieved at the end of the ray integration, indicating that the flow deformation also forces the wave tilt m/k toward to $U_z/\nabla_{\text{contr}}U$ but the wave packet does not have enough time to achieve wave capture.

The ray tracing results are consistent with the comment made by Bühler and McIntyre (2005) that when the mean flow gradient is varying along the ray, “the exponential straining of the wavenumber vector components will typically be slowed down but not eradicated—that is, capture will typically be delayed but not prevented.”

d. The effective Coriolis parameter due to the vortical motion

The dispersion relation based on the constant wind assumptions in GROGRAT could potentially cause

some inaccuracy in regions of strong vorticity. Kunze (1985) suggested a different dispersion relation that is based on the geostrophic wind assumption and found that the lower frequency limit of inertia–gravity waves in the region of strong vortical motion should be replaced by the effective Coriolis parameter $\sqrt{f(f + \zeta)}$ or its small-amplitude approximation $(f + \zeta/2)$, where ζ is the relative vertical vorticity. Although Kunze’s results have not been fully justified in a complex flow, the effective Coriolis parameter is helpful to understand the asymmetry of wave activities in the cyclonic and anticyclonic region.

Figure 11a shows that the effective Coriolis parameter in the vortex dipole increases in the cyclone but decreases in the anticyclone. Some very low-frequency waves (less than f) can be effectively trapped in the anticyclonic regions, where the effective Coriolis parameter reduces to $\sim 0.8f$ (Fig. 11b). In the cyclonic regions, near-inertial waves can encounter the horizontal critical level where the intrinsic frequency approaches the increased effective Coriolis parameter, which can potentially prevent waves from propagating into the cyclone and is partially responsible for the pronounced wave activities in the anticyclones. Nevertheless, the inclusion of the effective Coriolis parameter and more elaborate dispersion relation should not change the conclusions from the ray tracing analysis in this study, because the ray tracing is performed mostly in the jet exit region with small relative vorticity.

5. Dependence of wave amplitude on Rossby number

An important issue of spontaneously generated gravity waves is how the amplitude depends on the Rossby

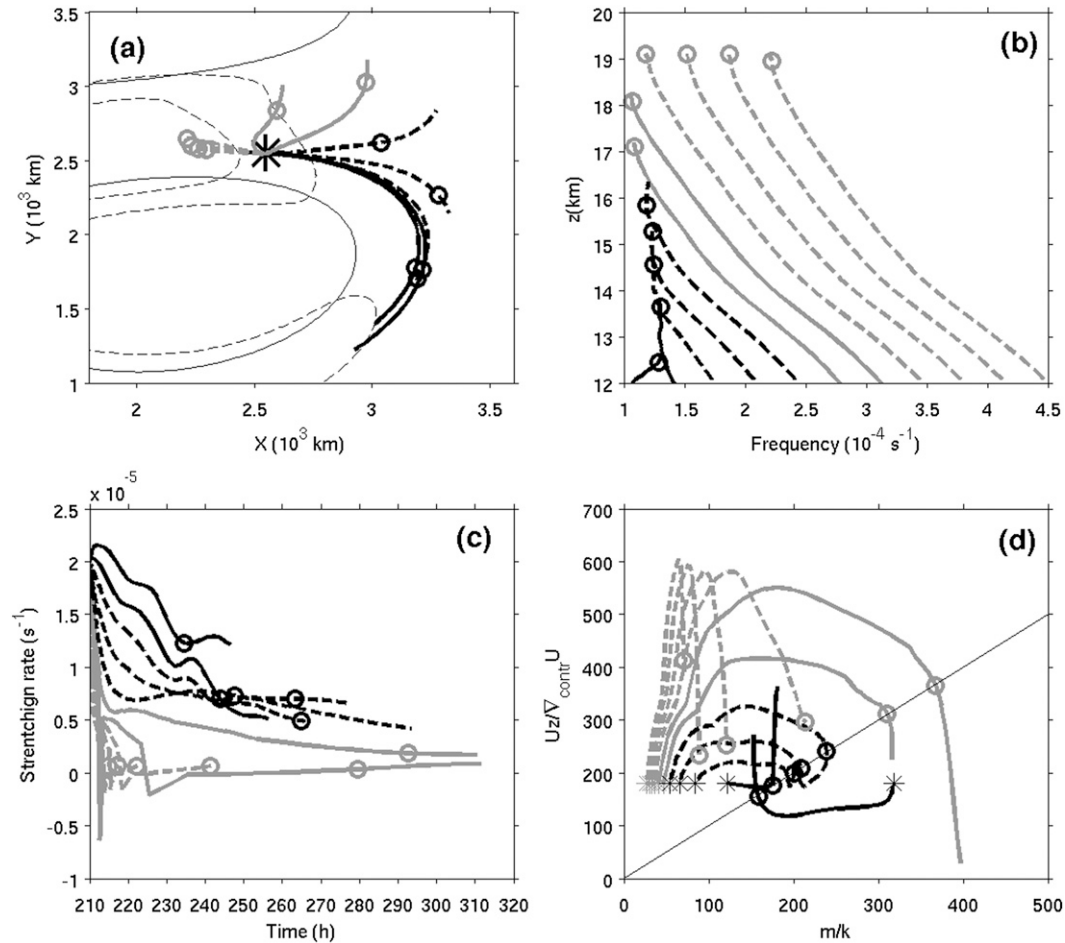


FIG. 10. (a) Ray paths projected onto the horizontal plane for wave packets with different initial intrinsic frequency [R1 ($f-1.5f$) dark solid lines; R2 ($1.5f-2.5f$), dashed lines; R3 ($2.5f-3.2f$), gray solid lines; and R4 ($3.2f-4.5f$), gray dashed lines), overlapped on the wind speed contours (dashed; 25 and 30 m s^{-1}) and perturbation potential temperature (thin solid; ± 4 K) at 12 km. (b) Variations of intrinsic frequency with respect to height. (c) Time evolution of the stretching rate. (d) Calculated vertical tilt (m/k) values compared with those predicted by the wave capture argument $U_z/\nabla_{\text{contr}}U$. The straight line in (d) is the diagonal line. The stars in (a) indicate the initial positions and in (d) the initial values of m/k and $U_z/\nabla_{\text{contr}}U$. The circles indicate that the wave packet that is the difference between $U_z/\nabla_{\text{contr}}U$ and m/k is minimal along the ray paths.

number. From analytical models, Vanneste and Yavneh (2004) demonstrated in a simple, analytically tractable flow that spontaneously emitted gravity waves were exponentially small in Rossby number when $\text{Ro} \ll 1$. Using the same asymptotic analysis method, Ólafsdóttir et al. (2008) recently discussed an example of exponentially weak emission of gravity waves. Plougonven et al. (2005) showed that instabilities of a baroclinic vertical shear that coupled inertia-gravity waves and balanced surface edge waves had growth rates that also increased exponentially with Rossby number. These are examples of exponentially small gravity waves in continuously stratified flow. They differ from gravity wave emission in a shallow water model studied by Ford (1994) and Ford et al. (2000) in that 1) the wave scales

are not necessarily much larger than that of the vortical flow and 2) the flow regime considered in Ford's results has a Rossby number larger than 1. The fundamental difference between gravity waves in vortex dipoles and spontaneous adjustment emission in Ford's studies are discussed in McIntyre (2009). From both the theoretical and practical point of views, it is important to quantify the wave-amplitude dependence on Rossby number. In the vortex dipole model, SMPZ07 simulated several vortex dipoles with different initial strengths and suggested that the wave motion has a power-law dependence on the maximum wind speed (essentially Rossby number). From laboratory observations of inertia-gravity waves emitted from balanced fluid flow, Williams et al. (2008) found that wave amplitude varies

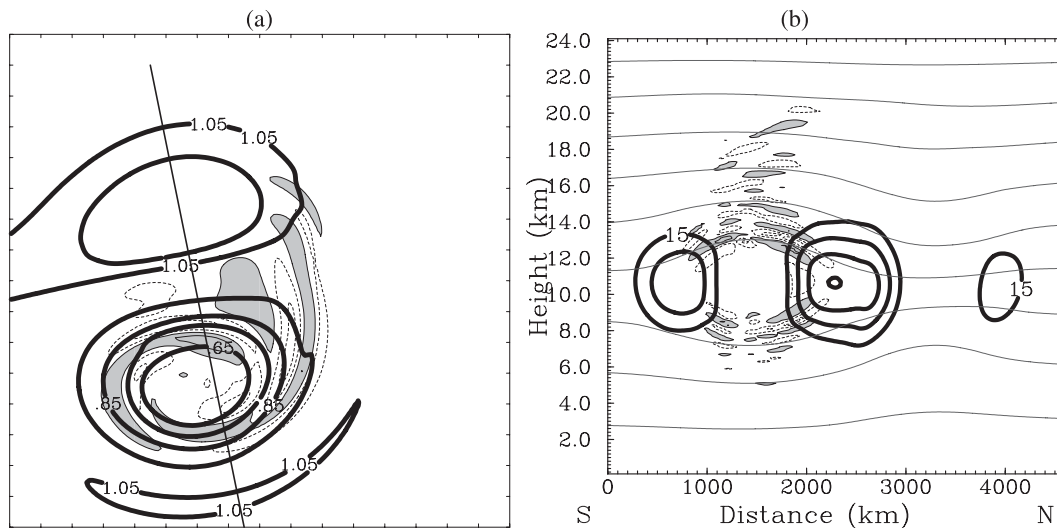


FIG. 11. (a) The effective Coriolis parameters ($CI = 0.05f$), horizontal divergence ($CI = 0.02 \times 10^{-4} \text{ s}^{-1}$; positive, shaded; negative, dashed), and wind vectors from MDJET valid at 210 h plotted at 12.5 km. (b) Horizontal divergence, wind speed ($CI = 5 \text{ m s}^{-1}$) and potential temperature ($CI = 6 \text{ K}$) in the vertical cross section indicated by thin line in (a).

linearly with Rossby number in the range 0.05–0.14. In this section, we examine gravity waves in slowly amplifying dipole jets and present an alternative way to quantify the dependence of wave amplitude on Rossby number.

The localized jets examined here emerge and amplify because of interactions between cyclones and anticyclones that are initially separated by a large distance and subsequently approach each other, developing into dipoles (pairs). This process of vortex paring seems to exclude the possibility of baroclinic instability, although the behavior of the balanced flow (e.g., vortex interactions) is not yet fully understood. In the following, we demonstrate that cyclones and anticyclones can develop into a vortex dipole and remain coherent for long times, while the jet strength amplifies with time.

Similar to the midlevel dipole experiment discussed in previous sections, the initial balanced flow is created from cosine-squared EPV perturbations, except that the initial distance between the cyclone and anticyclone is doubled to 3600 km. Because of the large distance between the vortices, the initially balanced flow contains no localized jet and has a Rossby number of ~ 0.06 . To further minimize the adjustment, the flow fields of the first 36 h are averaged, similar to SMPZ07, and the averaged flow fields are used to reinitialize the numerical model. Two additional experiments are performed in which the EPV perturbations are either increased or reduced by 20%. These three distant dipole experiments are referred to as medium, strong, and weak DISTJET; medium DISTJET will be discussed in detail

below. These DISTJET simulations are integrated over 50 days in a domain of 150×160 grid points with 90-km horizontal grid spacing. Another simulation with a large domain of $240 \times 250 \times 120$ grid points is also performed as a test for the sensitivity to boundary conditions in medium DISTJET; the results from medium DISTJET discussed below will not change in this large domain simulation. This suggests that boundary effects have very limited influence on the formation of the dipole vortex, as discussed below, although the exact mechanism is not clear at this time.

Figure 12 shows snapshots of the vortex dipoles at different times. The vortices approach each other with the distance between the vortex cores decreasing to ~ 3000 km at 240 h. Meanwhile, a slightly curved, localized jet with maximum wind speed $> 20 \text{ m s}^{-1}$ to the anticyclonic side of the dipole appears after ~ 240 h. Some wave bands located at the edge of the anticyclone gradually gain strength in the immediate exit region of the jet. Beginning at 360 h (Fig. 12c), a large-scale, four-cell pattern of divergence also gradually appears around the localized jet and strengthens with time. At 720 h (Fig. 12f), the maximum wind speed of the localized jet reaches $\sim 30 \text{ m s}^{-1}$, while the four cell divergence pattern and the embedded wave region expands with increasing wave amplitude. The increase of wind speed and decrease of distance renders a larger Rossby number (0.12) at this time, which is more than double that at the initial time.

Figure 13 further illustrates the embedded wave signals at 12.5 km by filtering out the large-scale divergence. A

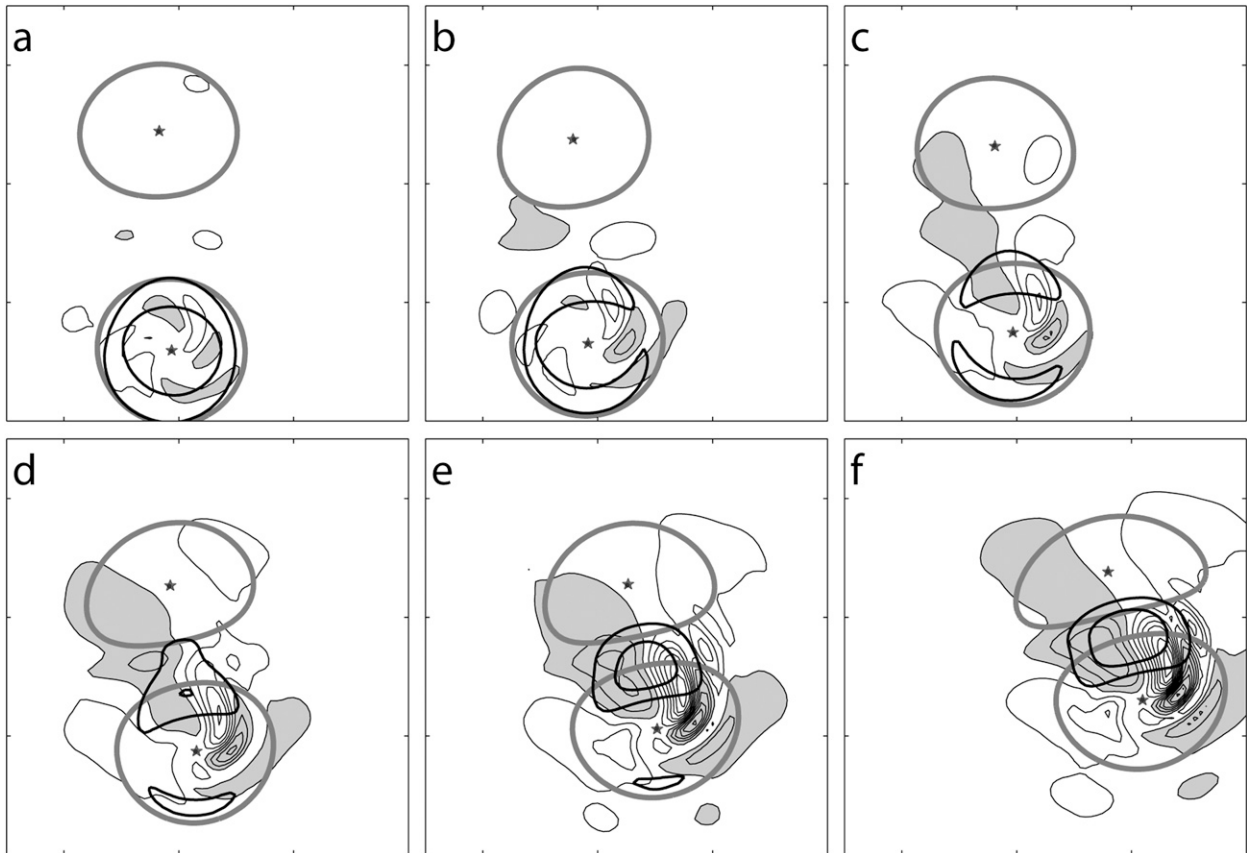


FIG. 12. Horizontal divergence ($CI = 0.02 \times 10^{-4} \text{ s}^{-1}$; positive, shaded; negative, dashed) is overlotted on perturbation EPV ($CI = \pm 1 \text{ PVU}$) and wind speed (blue lines; $CI = 5 \text{ m s}^{-1}$, values $< 20 \text{ m s}^{-1}$ omitted) on 90-km domains valid at (a) 120, (b) 240, (c) 360, (d) 480, (e) 600, and (f) 720 h. Stars indicate the defined vortex centers.

two-dimensional, high-pass digital filter is applied to horizontal divergence with a cutoff wavelength of 720 km. In general, more and stronger wave signals are found in the exit region of the slowly amplifying jet from DISTJET as the distance between the vortices becomes smaller.

Figure 14 shows Hovmöller diagrams of wind speed along the vortex cores at 11.5 km in the frame moving with the dipoles. The moving frame is defined much as in MDJET (Fig. 4), with the origin located midway between the vortex cores (which are indicated by dots in Fig. 12) and the x axis connecting the vortex cores. The localized jet between the vortices amplifies with time in all three experiments (Figs. 14a–c).

These evolving dipoles can be used to infer the dependence of wave amplitudes on jet strength and Rossby number because the vortex dipole flow evolves with different Rossby numbers. The Eulerian Rossby number is defined as $Ro = U/FL$, where U is the maximum wind speed and L is the distance between the vortex cores. However, other definitions of Rossby number can also be used—for instance, the local Rossby number

$Ro = \zeta/f$ as the ratio between the relative vorticity and planetary vorticity. The local Rossby number turns out to be less applicable here because it maximizes at the vortex core, which is away from the wave signatures in the exit region of the localized jet.

Figure 15 shows the time series of the Rossby number, the wave amplitude dependence on the maximum wind speed, and the Rossby number for all the three DISTJET simulations. Rossby numbers start below or around 0.05 and reach 0.15 in these simulations. Figure 15b also shows a linear fit between the natural logarithm of Rossby number and the natural logarithm of the maximum value of filtered divergence (with cutoff wavelength 720 km) at 12.5 km, which is used to represent the amplitude of gravity waves. The slopes of the best-fit lines in the medium, strong, and weak DISTJET are ~ 2.2 , 1.8, and 2.4, respectively. This suggests that the wave amplitude depends on Rossby number according to a power law Ro^β , with β falling between 1.8 and 2.4 when Ro falls in a small range of 0.05–0.15. To compare to $\beta = 4$ obtained in SMPZ07,

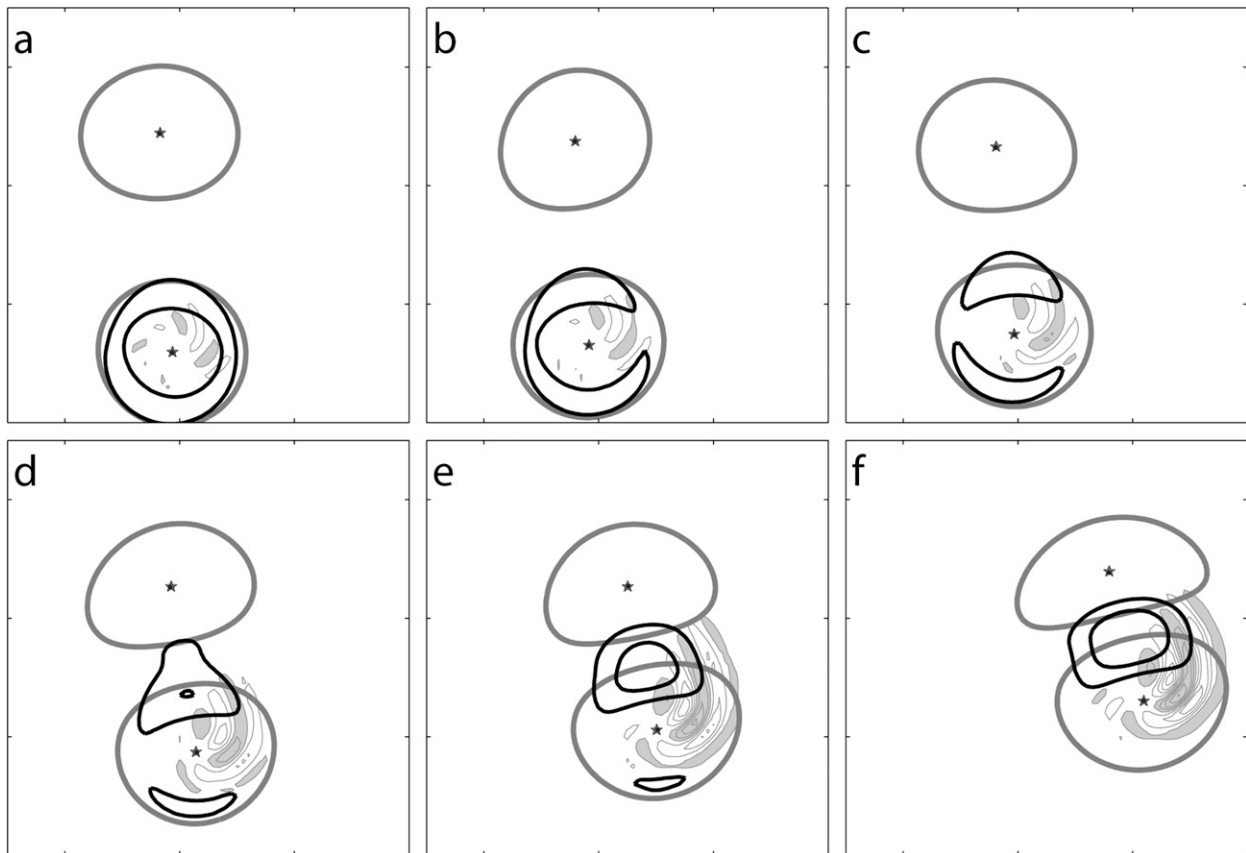


FIG. 13. As in Fig. 12, but a high-pass filter with cutoff wavelength 720 km is applied to horizontal divergence.

the estimated β values are recalculated using the maximum wind as the surrogate of Rossby number. Figure 15b shows the wave amplitude against the maximum winds for these three experiments. The recalculated β is found to increase to 6.0, 4.9, and 6, respectively. These values are greater than the value of 4.0 obtained in SMPZ07.

To test the resolution dependence of wave amplitude on the Rossby number, the medium-strength DISTJET experiment is performed with 30-km horizontal grid spacing. At this resolution, β increases to 2.76, greater than the value (2.2) in the 90-km simulations. If the maximum wind speed is taken as a surrogate for the Rossby number, β increases to 7.4, which is also significantly larger than the estimate (6.0) in the 90-km simulations. This increase of β probably arises because smaller-scale waves with stronger amplitude appear in the leading edge of the wave front in the simulation with higher resolution.

Note that consideration of the maximum filtered divergence is convenient but not necessarily the best measure of wave amplitude. We also consider other measures of wave magnitude, such as the maximum vertical veloc-

ity, the root-mean-square of the filtered divergence, and the vertical velocities. The estimated β is close to 2 (between 1.5 and 2.5) for most of these quantities. The uncertainties highlight the difficulty of estimating the wave amplitude dependence using a gridpoint numerical model.

From these distant dipole experiments with cyclones and anticyclones initially separated by a large distance, gravity waves are again simulated in the exit region of amplifying jets with increasing amplitude. These simulations further demonstrate that the waves are inherent features of vortex dipoles rather than remnants or adjustment from the initial conditions.

6. Summary and discussion

Owing to their simple structure and slowly evolving nature, vortex dipoles provide an ideal laboratory to explore fundamental mechanisms of spontaneous generation of gravity waves in a rotating, stratified flow. In this study, gravity wave generation and propagation from idealized vortex dipoles and jets are simulated with a nonhydrostatic, compressible mesoscale model. We examine two types of vortex dipoles, which are

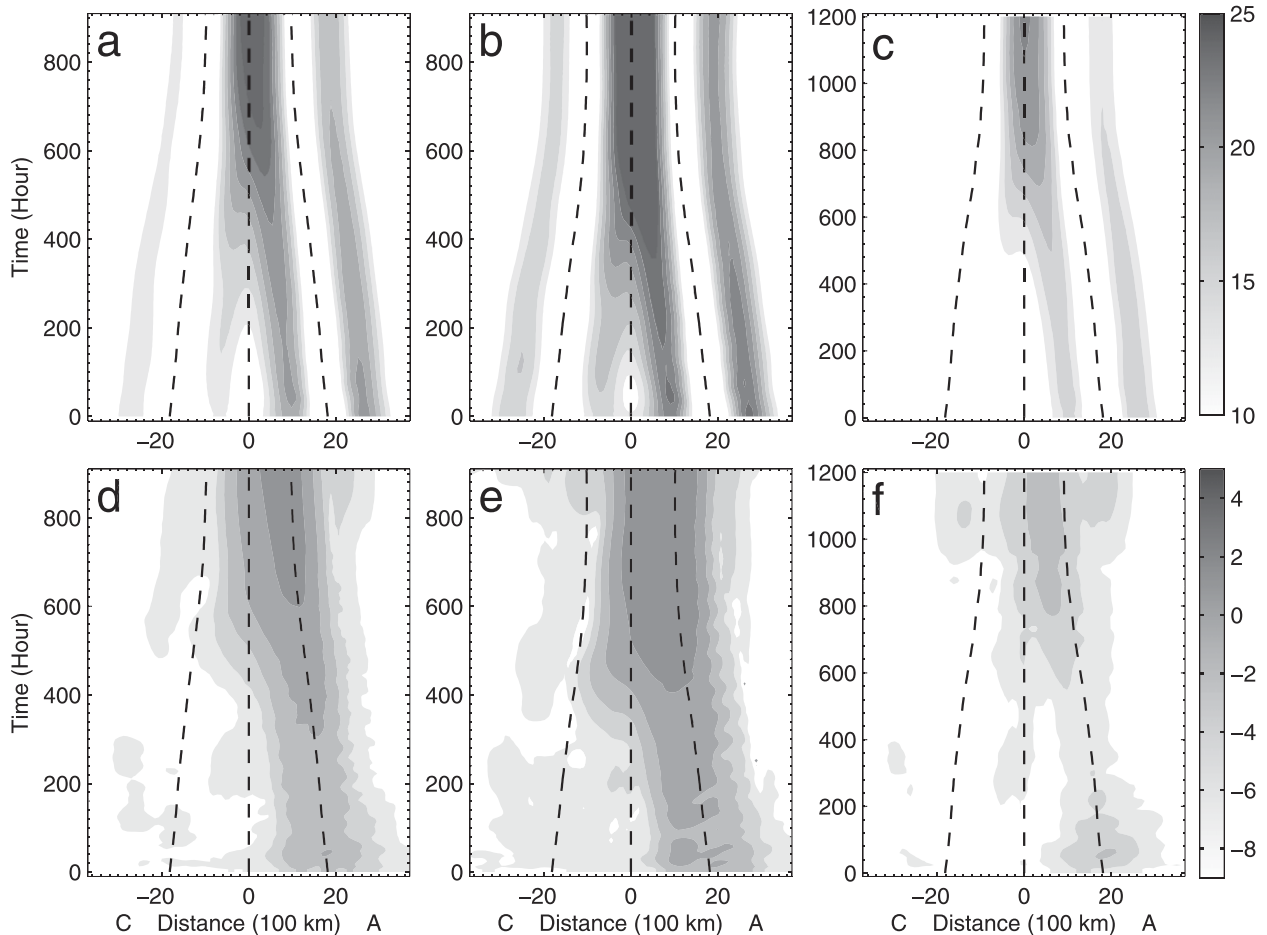


FIG. 14. (a)–(c) Hovmöller diagrams of wind speed ($CI = 1 \text{ m s}^{-1}$) along the centers of the cyclone and anticyclone for the three cases: (a) the medium dipole, (b) the strong dipole, and (c) the weak dipole. (d)–(f) Hovmöller diagrams of wave variance are plotted for (a)–(c), respectively. The centers of vortex dipoles are indicated by black dashed lines. Contours of wind speed less than 10 m s^{-1} are omitted.

initialized through potential vorticity inversion and have their maximum strength at either the surface or midlevel in a uniformly stratified atmosphere. In all our dipole simulations, a localized jet arises between the vortex pairs and inertia–gravity waves with intrinsic frequencies 1–2 times the Coriolis parameter appear in the jet exit region when the Rossby number of the flow exceeds 0.15. The gravity waves of interest are nearly stationary with respect to (or phase locked with) the localized jet. Gravity waves in the surface dipole are quite similar to those simulated in SMPZ07, whereas waves in the midlevel dipole are more pronounced near the anticyclone. We argue that the preferred appearance of gravity waves in these dipoles is due to the occurrence of the localized jets and their exit region. The phase locking between the jet and gravity waves suggests that these waves are closely related to the localized jet.

The propagation of jet exit region gravity waves in the midlevel dipole is investigated by a ray tracing model

(Mark and Eckermann 1995). The ray tracing analysis demonstrates that background flow deformation strongly influences the variation of wave characteristics along the ray paths: the horizontal and vertical wavelengths both decrease, the intrinsic frequency approaches the inertial frequency, and the intrinsic phase speed and vertical group velocity decrease toward zero. The ray tracing results indicate that wave capture plays a very important role in determining the wave structure. While the changes of wave characteristics are consistent with those that would precede wave capture, the ray tracing analysis also indicates that phase lines of the wave packet may not be parallel to lines of constant wind speed in the limited time. That is, wave capture may not occur for all wave packets because, as suggested in SMPZ07, some wave packets move through the strong deformation of the jet exit region sufficiently quickly that long-time asymptotic behavior (wave capture) may not be achieved.

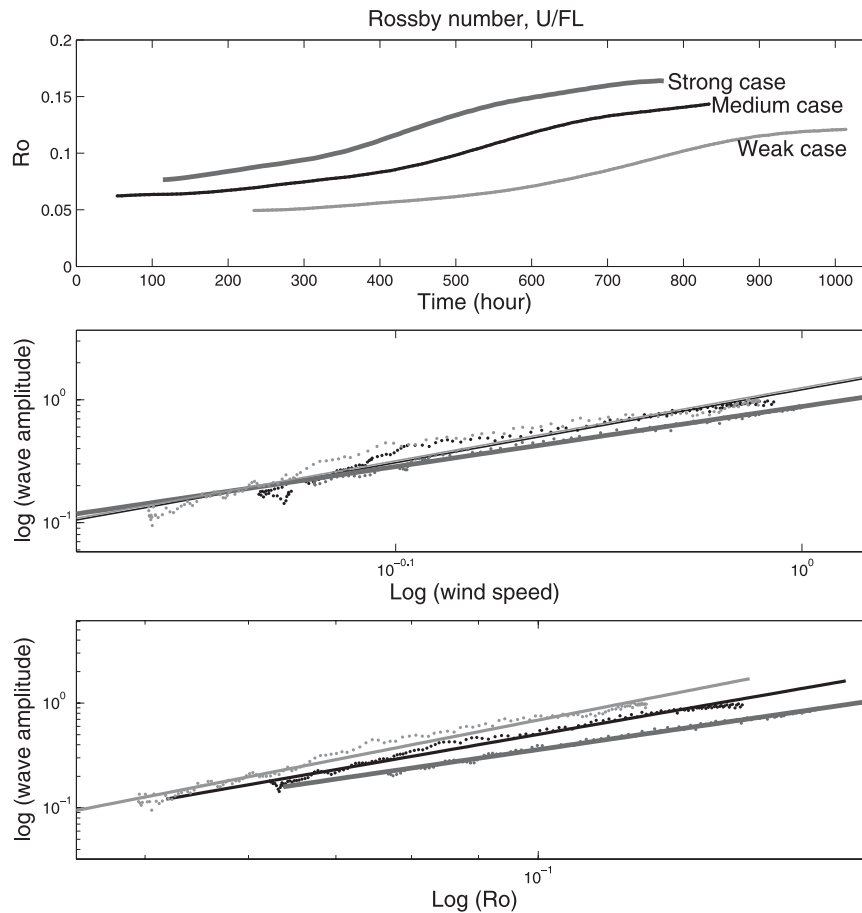


FIG. 15. (a) Time series of Eulerian Rossby number for three cases: the medium, strong, and weak distant dipoles. (b) The logarithm of the filtered maximum divergence is linearly regressed against the logarithm of Rossby number in each case in (a), with slope 2.2, 1.8, and 2.4, respectively, indicating the dependence of wave amplitude on Rossby number. (c) As in (b) except the x axis is the logarithm of the maximum wind speed in each case, with slope 6.0, 4.9, and 6.0, respectively.

The dependence of wave amplitude on the jet strength, and thus on the Rossby number, is also examined through distant dipole experiments. Here, the localized jets emerge and amplify because of interactions between cyclones and anticyclones that are initially separated by a large distance and subsequently approach each other, forming a jet in between. The amplitude of stationary gravity waves from these simulations increases roughly as the square of the Rossby number when Ro falls in a small range of 0.05–0.15 in the simulations using a 90-km grid spacing, but the rate of increase with Rossby number is noticeably larger when a smaller grid spacing is used. The resolution sensitivity likely results from smaller-scale waves with stronger amplitude appearing in the leading edge of the wave front in the higher-resolution simulation.

Our study, an extension of SMPZ07 and Viúdez (2007, 2008), documents inertia–gravity waves appearing in

the exit region of localized jets within vortex dipoles. We emphasize the role of jets in wave generation, propagation, and wave characteristics. However, several important questions still remain, among them 1) What precisely is the source mechanism of the gravity waves from the jets? Several hypotheses have been suggested in the literature (e.g., Ford et al. 2000, Zhang 2004, Viúdez 2007, SMPZ07, and McIntyre 2009). In particular, Viúdez (2007) suggested that the origin of the frontal wave packets is the large acceleration of the fluid particles as they move along the anticyclonic side of the dipole axis at shallow layers. However, quantitative assessment of these wave packets remains to be addressed. Other questions include 2) Can flow imbalance be useful to predict gravity wave generation? and 3) What is the effect of the gravity waves on the balanced flow? These are our current research topics.

Acknowledgments. The authors are thankful to Steve Eckermann for providing the GROGRAT ray tracing model and to Chris Davis for the PV inversion codes. The authors are grateful to Riwal Plougonven, Craig Epifanio, and David Muraki for discussions beneficial to this study, to Plougonven and two other anonymous reviewers for their insightful comments, which resulted in significant improvement in the revision, and to Matthew Rigney for proofreading an earlier version of the manuscript. The research was supported by NSF Grants ATM-0203238, 0618662, and 0904635.

APPENDIX

Reference State, PV Distribution, and Initial Conditions

a. The reference state

Assuming the basic state is horizontally homogeneous with uniform stratification $N^2 = g/\theta \partial\theta/\partial z = 2 \times 10^{-4} \text{ s}^{-2}$, we obtain the vertical distribution of potential temperature as function of height, $\theta = \theta_o \exp(N^2 z/g)$, and pressure by applying hydrostatic balance, $(p/p_o)^\kappa = g^2 \kappa / (R\theta_o N^2) [\exp(-N^2/gz) - 1] + 1$. At the surface, we apply the boundary condition with pressure $p_o = 1000 \text{ hpa}$ and $\theta_o = 300 \text{ K}$ when $z = 0$. The reference EPV in a resting atmosphere takes the form as a function of z only: $Q(z) = -gf\partial\theta/\partial p = -(fN^2/g)(\theta/\rho)$, where ρ is density obtained from the equation of state $\rho = p/(RT) = p^{1-\kappa} p_o^\kappa / (R\theta)$, p , θ , and f , the Coriolis parameter ($1 \times 10^{-4} \text{ s}^{-1}$).

b. EPV perturbation for the midlevel and surface vortex dipoles

Perturbation EPV introduced in the middle of the coarse domain is defined as the truncated cosine squared function with certain radius of influence R_o :

$$Q' = 0.75Q(z_o)[\cos^2(r_{10}\pi/2) - \cos^2(r_{20}\pi/2)],$$

where

$$r_{10} = \begin{cases} r_1, & \text{if } r_1 \leq 1, \\ 0; & \end{cases}$$

$$r_1 = \sqrt{(x - x_1)^2 + (y - y_1)^2 + \gamma \left[(z - z_o) \frac{\Delta x}{\Delta z} \right]^2} / R_o;$$

$$r_{20} = \begin{cases} r_2, & \text{if } r_2 \leq 1, \\ 0; & \end{cases} \quad \text{and}$$

$$r_2 = \sqrt{(x - x_2)^2 + (y - y_2)^2 + \gamma \left[(z - z_o) \frac{\Delta x}{\Delta z} \right]^2} / R_o.$$

The positive (negative) EPV anomaly is centered at (x_1, y_1, z_o) [(x_2, y_2, z_o)], with $x_1 = 60\Delta x$, $y_1 = 90\Delta y$, $x_2 = 60\Delta x$, $y_2 = 70\Delta y$, and $z_o = 58\Delta z = 11.6 \text{ km}$. These compact PV anomalies continuously drop to zero at the circle of radius $R_o = 20\Delta x = 1800 \text{ km}$ at the level of z_o . The vertical penetration of PV anomalies is controlled by the parameter $\gamma = 0.64$ such that they achieve a maximum depth of 10 km at the center (x_1, y_1) or (x_2, y_2) .

Perturbed potential temperature is introduced in a similar way with the same cosine squared function: $\theta(z = 0) = 25[\cos^2(r_{10}\pi/2) - \cos^2(r_{20}\pi/2)]$.

c. Scaling of Ertel potential vorticity

Ignoring the horizontal wind shear, Ertel PV can be written as

$$Q = \frac{g}{\rho\theta_o} \left(fN^2 + \zeta N^2 + f \frac{\partial b}{\partial z} + \zeta \frac{\partial b}{\partial z} + \zeta_x \frac{\partial b}{\partial x} + \zeta_y \frac{\partial b}{\partial y} \right).$$

Introducing horizontal and vertical scales L and H and wind scale U , relatively vorticity ζ and buoyancy $b = g/\theta_o \partial\theta'/\partial z$ are scaled as $\zeta \sim U/L$, $b \sim UFL/H$. It can be shown that the ratios of last five terms to the first term (background PV) are

$$\frac{\zeta N^2}{fN^2} \sim \text{Ro}, \quad \frac{f \frac{\partial b}{\partial z}}{fN^2} \sim \frac{\text{Ro}}{\text{Bu}}, \quad \text{and}$$

$$\frac{\left(\zeta \frac{\partial b}{\partial z}, \zeta_x \frac{\partial b}{\partial x}, \zeta_y \frac{\partial b}{\partial y} \right)}{fN^2} \sim \frac{\text{Ro}^2}{\text{Bu}}.$$

The linear terms (terms 2 and 3) are both scaled as Ro assuming the Burger number $\text{Bu} \sim 1$. The Rossby number is of the small order $\text{Ro}:O(1)$. The last three terms are the next order of corrections Ro^2 .

REFERENCES

Badulin, S. I., and V. I. Shrira, 1993: On the irreversibility of internal-wave dynamics due to wave trapping by mean flow inhomogeneities. Part 1. Local analysis. *J. Fluid Mech.*, **251**, 21–53.

Bühler, O., and M. E. McIntyre, 2005: Wave capture and wave–vortex duality. *J. Fluid Mech.*, **534**, 67–95.

Davis, C. A., and K. A. Emanuel, 1991: Potential vorticity diagnosis of cyclogenesis. *Mon. Wea. Rev.*, **119**, 1929–1953.

Dudhia, J., 1993: A nonhydrostatic version of the Penn State NCAR mesoscale model: Validation tests and simulation of an Atlantic cyclone and cold front. *Mon. Wea. Rev.*, **121**, 1493–1513.

- Dunkerton, T. J., and N. Butchart, 1984: Propagation and selective transmission of inertial gravity waves in sudden warming. *J. Atmos. Sci.*, **41**, 1443–1460.
- Eckermann, S. D., and C. J. Marks, 1997: GROGRAT: A new model of the global propagation and dissipation of atmospheric gravity waves. *Adv. Space Res.*, **20**, 1253–1256.
- Flierl, G. R., 1987: Isolated eddy models in geophysics. *Annu. Rev. Fluid Mech.*, **19**, 493–530.
- Ford, R., 1994: Gravity wave radiation from vortex trains in rotating shallow water. *J. Fluid Mech.*, **281**, 81–118.
- , M. E. McIntyre, and W. A. Norton, 2000: Balance and the slow quasimanifold: Some explicit results. *J. Atmos. Sci.*, **57**, 1236–1254.
- Fritts, D. C., and M. J. Alexander, 2003: Gravity wave dynamics and effects in the middle atmosphere. *Rev. Geophys.*, **41**, 1003–1063.
- Grell, G. A., J. Dudhia, and D. R. Stauffer, 1994: A description of the fifth-generation Penn State/NCAR mesoscale model (MM5). NCAR Tech. Note, NCAR/TN-398+STR, 122 pp.
- Hoskins, B. J., M. E. McIntyre, and A. W. Robertson, 1985: On the use and significance of isentropic potential vorticity maps. *Quart. J. Roy. Meteor. Soc.*, **111**, 877–946.
- Kunze, E., 1985: Near-inertial wave propagation in geostrophic shear. *J. Phys. Oceanogr.*, **15**, 544–565.
- Lighthill, M. J., 1978: *Waves in Fluids*. Cambridge University Press, 496 pp.
- Lin, Y., and F. Zhang, 2008: Tracking gravity waves in baroclinic jet-front systems. *J. Atmos. Sci.*, **65**, 2402–2415.
- Marks, C. J., and S. D. Eckermann, 1995: A three-dimensional nonhydrostatic ray-tracing model for gravity waves: Formulation and preliminary results for the middle atmosphere. *J. Atmos. Sci.*, **52**, 1959–1984.
- McIntyre, M. E., 2009: Spontaneous imbalance and hybrid vortex-gravity structures. *J. Atmos. Sci.*, **66**, 1315–1326.
- Ólafsdóttir, E. I., A. B. Olde Daalhuis, and J. Vanneste, 2008: Inertia-gravity-wave radiation by a sheared vortex. *J. Fluid Mech.*, **596**, 169–189.
- O’Sullivan, D., and T. J. Dunkerton, 1995: Generation of inertia-gravity waves in a simulated life cycle of baroclinic instability. *J. Atmos. Sci.*, **52**, 3695–3716.
- Plougonven, R., and H. Teitelbaum, 2003: Comparison of a large-scale inertia-gravity wave as seen in the ECMWF analyses and from radiosondes. *Geophys. Res. Lett.*, **30**, 1954, doi:10.1029/2003GL017716.
- , and C. Snyder, 2005: Gravity waves excited by jets: Propagation versus generation. *Geophys. Res. Lett.*, **32**, L18802, doi:10.1029/2005GL023730.
- , and —, 2007: Inertia-gravity waves spontaneously generated by jets and fronts. Part I: Different baroclinic life cycles. *J. Atmos. Sci.*, **64**, 2502–2520.
- , and F. Zhang, 2007: On the forcing of inertia-gravity waves by synoptic-scale flows. *J. Atmos. Sci.*, **64**, 1737–1742.
- , D. J. Muraki, and C. Snyder, 2005: A baroclinic instability that couples balanced motions and gravity waves. *J. Atmos. Sci.*, **62**, 1545–1559.
- Rotunno, R., D. J. Muraki, and C. Snyder, 2000: Unstable baroclinic waves beyond quasigeostrophic theory. *J. Atmos. Sci.*, **57**, 3285–3295.
- Sato, K., 1994: A statistical study of the structure, saturation, and sources of inertio-gravity waves in the lower stratosphere observed with the MU radar. *J. Atmos. Terr. Phys.*, **56**, 755–774.
- Snyder, C., D. J. Muraki, R. Plougonven, and F. Zhang, 2007: Inertia-gravity waves generated within a dipole vortex. *J. Atmos. Sci.*, **64**, 4417–4431.
- Staquet, C., and J. Sommeria, 2002: Internal gravity waves: From instabilities to turbulence. *Annu. Rev. Fluid Mech.*, **34**, 559–593.
- Uccellini, L. W., and S. E. Koch, 1987: The synoptic setting and possible source mechanisms for mesoscale gravity wave events. *Mon. Wea. Rev.*, **115**, 721–729.
- Vanneste, J., and I. Yavneh, 2004: Exponentially small inertia-gravity waves and the breakdown of quasigeostrophic balance. *J. Atmos. Sci.*, **61**, 211–223.
- Viúdez, A., 2006: Spiral patterns of inertia-gravity waves in geophysical flows. *J. Fluid Mech.*, **562**, 73–82.
- , 2007: The origin of the stationary frontal wave packet spontaneously generated in rotating stratified vortex dipoles. *J. Fluid Mech.*, **593**, 359–383.
- , 2008: The stationary frontal wave packet spontaneously generated in mesoscale dipoles. *J. Phys. Oceanogr.*, **38**, 243–256.
- Wang, S., and F. Zhang, 2007: Sensitivity of mesoscale gravity waves to the baroclinicity of jet-front systems. *Mon. Wea. Rev.*, **135**, 670–688.
- Williams, P. D., T. W. N. Haine, and P. L. Read, 2008: Inertia-gravity waves emitted from balanced flow: Observations, properties, and consequences. *J. Atmos. Sci.*, **65**, 3543–3556.
- Wu, D. L., and F. Zhang, 2004: A study of mesoscale gravity waves over the North Atlantic with satellite observations and a mesoscale model. *J. Geophys. Res.*, **109**, D22104, doi:10.1029/2004JD005090.
- Zhang, F., 2004: Generation of mesoscale gravity waves in the upper-tropospheric jet-front systems. *J. Atmos. Sci.*, **61**, 440–457.
- , S. E. Koch, C. A. Davis, and M. L. Kaplan, 2000: A survey of unbalanced flow diagnostics and their application. *Adv. Atmos. Sci.*, **17**, 165–183.
- , —, —, and —, 2001: Wavelet analysis and the governing dynamics of a large-amplitude gravity wave event along the East Coast of the United States. *Quart. J. Roy. Meteor. Soc.*, **127**, 2209–2245.